

# **Micro-scale testing and micromechanical modelling for high cycle fatigue of CoCr stent material.**

C.A. Sweeney<sup>a,\*</sup>, B. O'Brien<sup>b</sup>, F.P.E. Dunne<sup>c</sup>, P.E. McHugh<sup>b</sup>, S.B. Leen<sup>a</sup>

<sup>a</sup>*Mechanical Engineering, College of Engineering and Informatics, National University of Ireland Galway, Ireland*

<sup>b</sup>*Biomedical Engineering, College of Engineering and Informatics, National University of Ireland Galway, Ireland*

<sup>c</sup>*Department of Materials, Imperial College London*

*\*Corresponding author: Tel: +353 (0)91 493020; Fax: +353 (0)91 563991;  
E-mail: c.sweeney4@nuigalway.ie*

## **Abstract**

This paper presents a framework of experimental testing and crystal plasticity micromechanics for high cycle fatigue (HCF) of micro-scale L605 CoCr stent material. Micro-scale specimens, representative of stent struts, are manufactured via laser micro-machining and electro-polishing from biomedical grade CoCr alloy foil. Crystal plasticity models of the micro-specimens are developed using a length scale-dependent, strain-gradient constitutive model and a phenomenological (power-law) constitutive model, calibrated from monotonic and cyclic plasticity test data. Experimental microstructural characterization of the grain morphology and precipitate distributions is used as input for the polycrystalline finite element (FE) morphologies. Two microstructure-sensitive fatigue indicator parameters are applied, using local and non-local (grain-averaged) implementations, for the phenomenological and length scale-dependent models, respectively, to predict fatigue crack initiation (FCI) in the HCF experiments.

*Keywords:* high cycle fatigue, CoCr alloy, crystal plasticity, finite element

## **1. Introduction**

The issue of premature fracture of stents has come to the fore in recent times due to the evolution of drug-eluting stents (DESs) e.g. [1–3]. Fractures were previously concealed by growth of neointima over stent struts and often went unnoticed as the tissue-growth provided support at the site of the fracture and provided coverage from the blood flow [4,5]. The prevention of restenosis with DESs resulted in the exposure of stent fracture sites. High cycle fatigue is a cause of premature stent fracture. For example, slip bands reported by Halwani et al. [1] at sites of stent fracture support the case for HCF as the probable fracture mechanism. For micro-scale devices, for which dimensions are comparable in size to microstructural features, such as stents, crack propagation is expected to play only a small role, i.e. it is expected that fatigue life is dominated by fatigue crack initiation (FCI) and microstructurally small crack growth, as the specimen cross-section is compromised before the later stages of crack growth. Therefore, the dependence of fatigue performance on microstructural attributes is expected to increase for such devices. It follows that microstructure-based approaches are needed to truly assess stent fatigue performance.

Some studies have attempted to address this need, including the work of Marrey et al. [6] in which an El-Haddad type approach [7], accounting for crack sizes which are below a microstructural threshold, was applied to fracture mechanics calculations for a CoCr alloy stent, facilitating prediction of the minimum size of an initial flaw in a stent strut which could cause failure. A key conclusion of this work was the need for microstructural modelling in stent fatigue assessment. Barrera et al. [8] adopted the Dang Van criterion for prediction of fatigue performance of a 316L SS stent, using shear and hydrostatic stresses evaluated at the mesoscopic level. The authors have previously applied a crystal plasticity (CP) approach (i.e. modelling of slip on individual slips systems in the crystal lattice of discrete grains) to fatigue

assessment of 316L stainless steel [9] and L605 CoCr alloy stents [10], demonstrating the ability to capture the effect of microstructural inhomogeneity and illustrating scope for the CP framework as a tool for fatigue design of stent geometries. Patient-specific modelling, such as presented by Schievano et al. [11], can offer a means of validation via direct comparison between models and deformed stents, extracted from real patient vessel geometries. However, the procurement of the required data is difficult and this approach may be less applicable to the initial stages of stent fatigue design, prior to approval for *in vivo* operation. Representative testing can be used for experimental validation of models at the design stage. Wiersma et al. [12,13] applied the theory of critical distances to prediction of the HCF behaviour of 316L stent material and validated predictions via comparison against HCF tests on micro-specimens with features representative of stents. Pelton et al. [14] demonstrated that a subcomponent micro-specimen exhibited similar fatigue behaviour to a full stent, effectively endorsing the concept of a representative test as a simplified experiment against which predictive models can be calibrated and validated.

As mentioned previously, crack initiation is expected to dominate over propagation in HCF, particularly in the case of micro-scale components, and it has been firmly established that FCI is a microstructurally-driven phenomenon [15–17]. Sangid [18] provides a comprehensive description of the build-up of dislocations and development of energy minimising dislocation structures leading to the formation of persistent slip bands, and subsequent crack initiation at the slip band-matrix interface. It is clear that microstructure-sensitive modelling methodologies are needed for the capture of the phenomena leading to FCI and, thus, HCF failure. Sangid et al. [19–21] have developed a dislocation-driven criterion for the prediction of FCI based on the stability of an energy balance for PSB formation, including terms for dislocation-grain boundary interaction determined via

atomistic simulations. Microstructure-sensitive fatigue indicator parameters (FIPs) coupled with CP modelling represents another approach. Studies by Przybyla and McDowell [22,23] used such an approach to investigate the influence of different attributes on the development of extreme values of FIPs, considered to be drivers of FCI, in HCF. These studies used large numbers of statistical volume elements (SVEs) to develop reliable probability functions for different microstructural attributes; the SVEs used were large enough such that FIPs at a point were unaffected by microstructure variations at a distance equal to the size of the SVE. The SVEs differ from representative volume elements (RVEs) in that the macroscopic response of SVEs may vary. In a previous study by the authors [24], the use of a CP-based microstructure model, coupled with the effective plastic strain FIP,  $p$ , was demonstrated for prediction of FCI locations in HCF of ferritic steel, four-point bending specimens. This study did not, however, investigate the ability of the framework to predict number of cycles to FCI. Manonukul and Dunne [25] postulated that the critical value of the effective plastic strain FIP, at which FCI is predicted to occur, is a material constant and have consolidated this concept via prediction of fatigue behaviour for a range of loading conditions, across both low cycle fatigue (LCF) and HCF regimes, including mean stress effects, for a nickel-base alloy. A crystallographic work parameter [26],  $W$ , has also been successfully used to predict the experimentally-observed FCI site for an austenitic steel [27].

The HCF performance of the L605 CoCr alloy, commonly used in cardiovascular stents, is investigated in this study, both experimentally and computationally, via a micromechanical framework. The study presented here adopts the concept of representative testing for stent fatigue loading. The representative testing facilitates validation of the micromechanical framework at a physical length scale consistent with the stent application, and for the HCF regime. L605 foil micro-specimens are manufactured and tested under HCF loading

conditions, and microscopy is carried out on the foil to aid in generation of realistic cross-section polycrystalline models for the foil specimens. The micromechanical framework used for HCF prediction has been developed and calibrated in previous works [10,28] for the LCF fatigue behaviour of the L605 alloy, and is hypothesised to predict fatigue behaviour across both LCF and HCF regimes. Two CP models are investigated and compared within the micromechanical framework for describing the material constitutive behaviour. The first is a physically-based strain-gradient CP model, which has been calibrated against cyclic plasticity data for as-received, fine-grain ( $d = 32 \mu\text{m}$ ) L605 material in previous work [28] and, with the same calibrated constants, has been shown to also capture the behaviour of heat-treated, coarse grain ( $d = 243 \mu\text{m}$ ) material. A phenomenological power-law constitutive model, previously calibrated against both monotonic and cyclic plasticity data, and applied to the assessment of a stent fatigue design for the L605 alloy [10], is also investigated. Two microstructure-sensitive FIPs, effective plastic strain,  $p$ , and crystallographic work,  $W$ , are implemented for the prediction of the number of cycles to crack initiation,  $N_i$ , for HCF behaviour, based on critical FIP values calibrated and validated from macro-scale LCF test data [10,28], and the predictions are compared with the experimental stress-life data. The micromechanical framework presented and validated here for stent fatigue design addresses an outstanding predictive need, highlighted by Marrey et al. [6], for HCF of CoCr alloy stents.

## **2. Experiments**

The experimental test program for the L605 CoCr alloy foil is discussed in this section, including microstructural characterisation of the foil and preparation and testing of foil fatigue specimens. The L605 foil used in the study was supplied in  $100 \times 100$  mm sheets with thickness of 265 to 270  $\mu\text{m}$  by Goodfellow Cambridge Limited, with chemical composition

of 50 wt % cobalt, 20 wt % chromium, 15 wt % tungsten, 10 wt % nickel, 3 wt % iron and 2 wt % manganese.

### **2.1. Microscopy**

Microstructural characterization of the foil was carried out to provide data for generation of microstructure FE geometries, including grain size statistics, precipitate statistics and crystallographic texture. Optical microscopy was first carried out to determine the grain structure in the foil. An etching solution of 100 ml HCl and 5 ml 30% H<sub>2</sub>O<sub>2</sub> was used, as described for the macro-scale CoCr material in [10,28]. Optical micrographs of the foil are shown in Fig. 1 (a), where three directions, corresponding to the flat surface and two perpendicular edges, are investigated. A Matlab program was written to extract grain area statistics from the micrographs; the program calculates individual grain areas based on the number of pixels in a polygon, defined by the grain boundaries, and proceeds to generate a distribution of grain areas. As seen from the micrographs of Fig. 1 (a) and the grain area distributions of Fig. 1 (b), a similar grain morphology is observed for all three directions; it appears the microstructure is equiaxed. As in previous studies [10,28], an approximation of hexagonal grains is adopted to extract a grain size distribution; a hexagon-based conversion is applied to each grain measurement, whereby the grain size of a hexagonal grain (flat-to-flat dimension), with area equivalent to the measured grain area, is identified. The foil material is found to have an average grain size of 38  $\mu\text{m}$ , corresponding to the average grain size for equivalent hexagonal grains. Additionally, twin boundaries can be observed in the micrographs for the as-received foil, attributed to annealing carried out by the manufacturer.

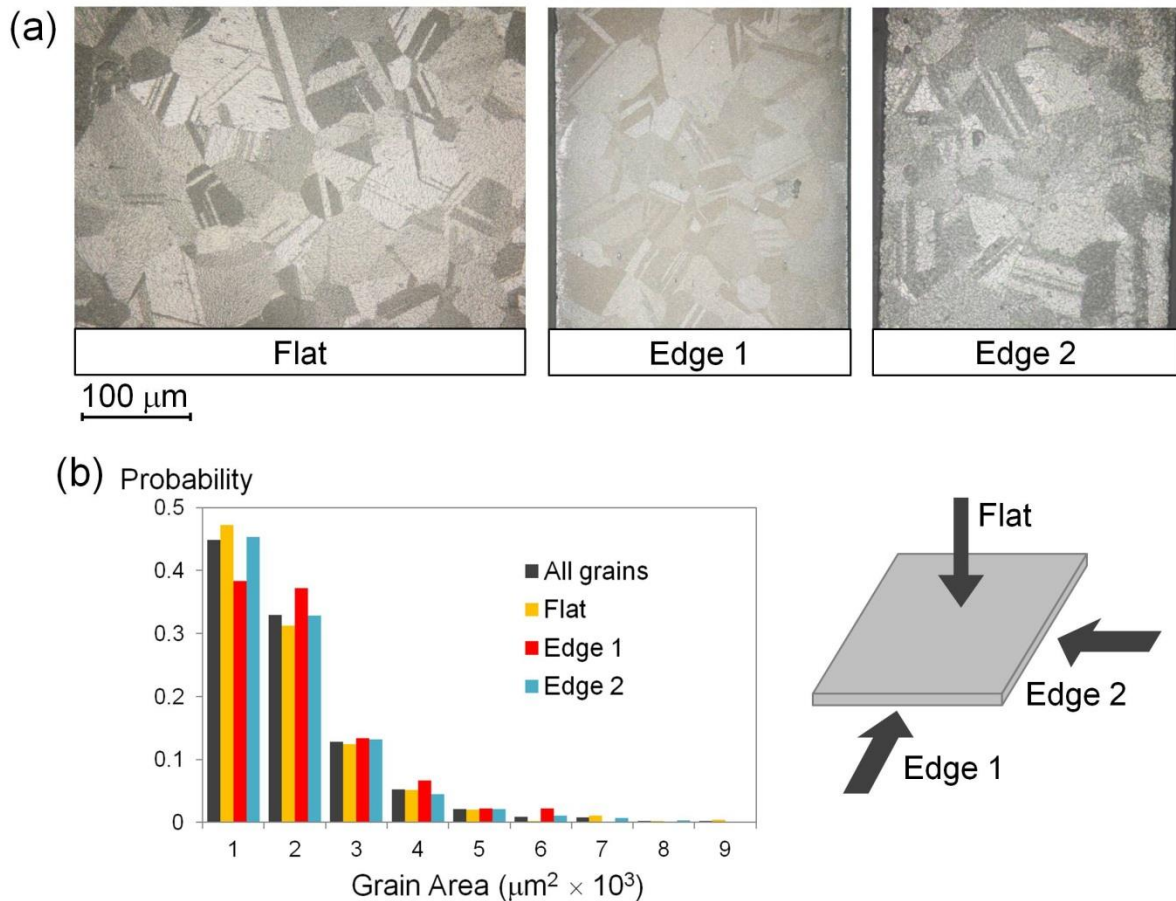


**Figure 1** (a) Optical micrographs of the etched foil in the flat and two edge directions and (b) measured grain area distributions for the foil.

Scanning electron microscopy (SEM) is employed both for investigation of crystallographic texture and characterization of particles in the microstructure. The electron backscatter diffraction (EBSD) technique is coupled with SEM, to produce the EBSD crystallographic orientation maps, shown in Fig. 2 (a), for the three directions of Fig. 1. A lack of crystallographic texture is observed, due to heat treatment of the foil, indicating that the grains have random crystallographic orientation. Without heat-treatment of the foil, a strong crystallographic texture, developed during the manufacturing process, would still exist. If this were the case, any attempt to simulate the foil fatigue behaviour would require inclusion of such texture in the model, as it would have an effect on the mechanical performance of the

foil. For example, Mineur et al. [29] observed a softer cyclic response for fatigue specimens machined from 316L (fcc) rolled sheet material to favour the  $\langle 110 \rangle$  direction.

SEM is also used to identify precipitates in the microstructure, as shown in Fig. 2 (b), where energy dispersive x-ray (EDX) analysis is employed to confirm a tungsten rich composition, as for precipitates observed in as-received L605 bar material in previous work [10]. A Matlab program was written to extract statistics for precipitate area and frequency from micrographs, indicating an average precipitate area of  $1.51 \mu\text{m}^2$  and area fraction of 0.34%.

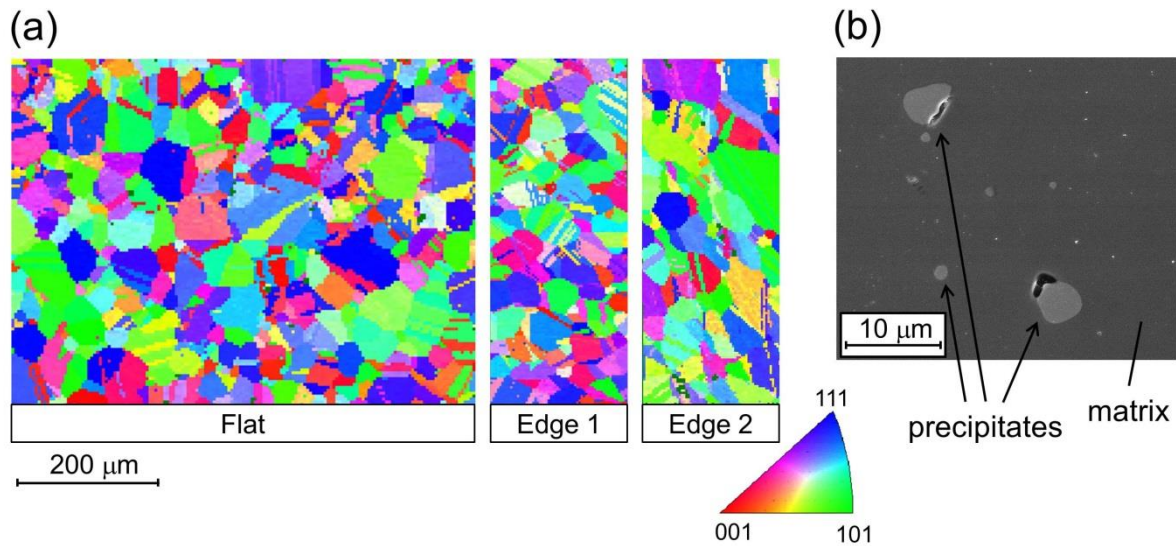


**Figure 2** (a) EBSD orientation maps for the three direction of the L605 foil and (b) SEM image showing precipitates (light grey) within the L605 matrix (dark grey).

## ***2.2. Fatigue Specimen Preparation***

Micro-scale foil specimens were manufactured which are scale-consistent with stent struts. Microscopy results from the previous section demonstrate the lack of morphological or crystallographic texture in the foil, thus eliminating concerns over directionality in the material itself. The specimens were manufactured via laser-cutting and electro-polishing (EP). The specimen drawing used for the laser-cutting of foil specimens is given in Fig. 3 (a)



and (b), where consideration of laser beam spot size and material removal in EP is taken into account. The specimen design, based on the work of Donnelly [30], has a dogbone-type gauge region, with uniform gauge length and fillets at each end to a larger cross-section. A second fillet is used to transition to the gripped cross-section. Support struts are included to allow ease of handling and structural integrity before testing, and can be snipped once the specimen is loaded in the fatigue tester. A laser-cut specimen is shown in Fig. 3 (c), in which the support struts are labelled. The laser-cutting was carried out on a Trumpf TruMicro 5050 picosecond laser, which minimizes heat input and, therefore, gives a small heat-affected zone. The laser has a fundamental wavelength of 1030 nm. 2100 passes at a rate of 0.5 m/s were completed for each specimen using a final wavelength of 343 nm and beam power, repetition rate and pulse energy of 5.6-5.7 W, 200 Hz and 120  $\mu$ J, respectively.

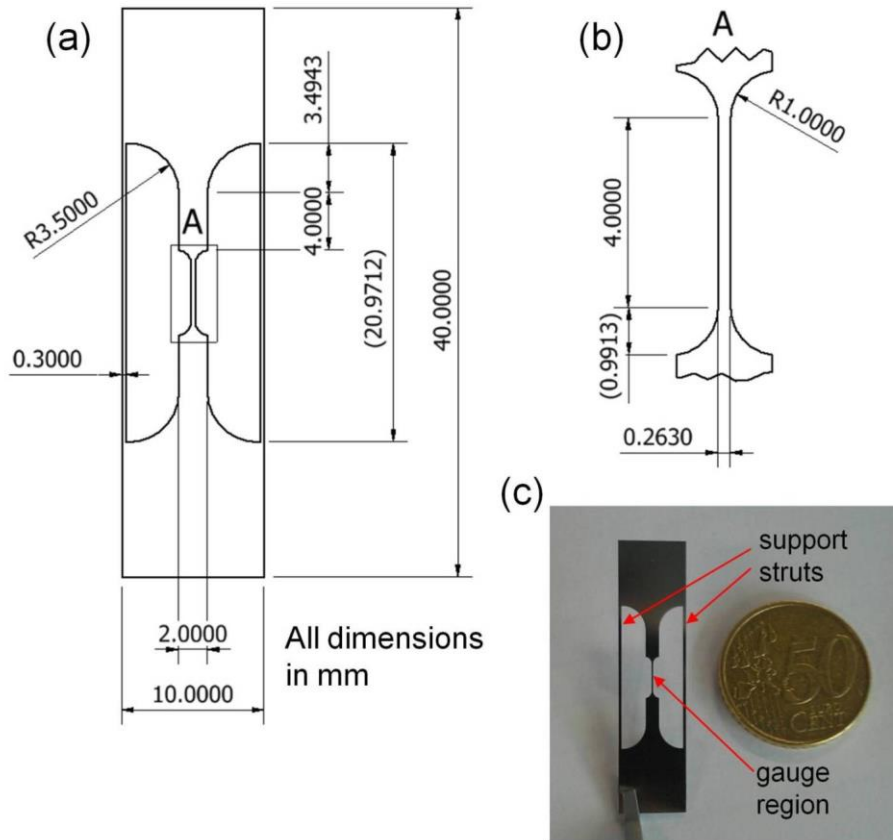


**Figure 3** (a) Drawing of foil fatigue specimen with a magnified view of the gauge region in (b) and (c) comparison of a laser-cut specimen with a 50 cent euro coin.

Electro-polishing (EP) is required to remove the heat-affected zone and any surface oxides created during laser-cutting, and to provide a smooth surface. A number of studies have looked at the electro-polishing of L605 for stent applications, reporting the use of various EP solutions, including a hydrofluoric and nitric acid solution [31], phosphoric acid of different concentrations [32], a perchloric and acetic acid solution [33] and a sulfuric and phosphoric acid solution [34]. Various optimal temperatures, EP times and current-voltage settings have also been reported. Three studies report polishing temperatures of around 55 °C [31,33,34], while another reports more uniform EP rates at 0 °C [32]. An EP approach based on the work of Kaufmann et al. [34] is adopted here. The specimens were first cleaned ultrasonically in deionised water after laser-cutting. EP was then applied to each specimen, followed by

rinsing with alcohol and then ultrasonic cleaning in deionised water. The EP solution was comprised of 45 vol% sulfuric acid, 50 vol% phosphoric acid and 5 vol% water. A schematic of the EP setup is provided in Fig. 4. The specimen and a piece of stainless steel are connected to the anode and cathode of a 1.5-10 V/10 A power supply, respectively, and agitation is provided via a magnetic stirrer.

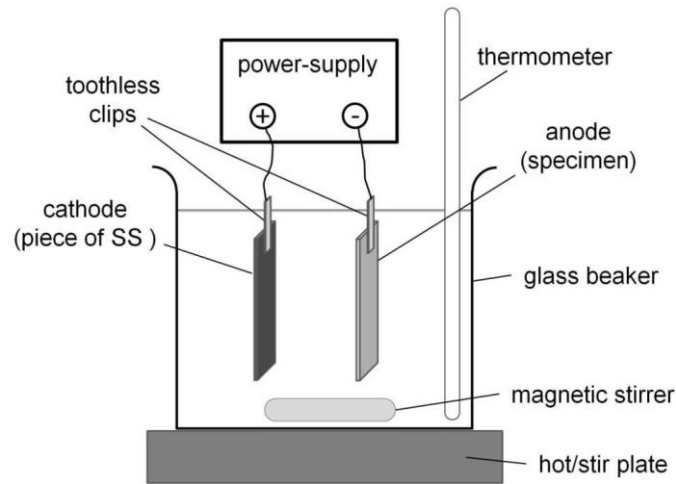


**Figure 4** Schematic of set-up for electro-polishing of laser-cut specimens.

EP trials were initially carried out at 55 °C with a current density of 1-1.5 A/cm<sup>2</sup> as prescribed by Kaufmann et al. [34]. However, an uncontrolled EP process was observed at these settings with non-uniform material removal resulting in pitting. Therefore, the temperature and current were reduced until a more controlled EP process was observed. The final temperature and current density settings of 25 °C and 0.66 A/cm<sup>2</sup>, respectively, were used, while it was found that an EP time of 10 minutes was required to remove visible surface dross from the laser-cutting process. Optical images of the gauge region of a specimen before and after EP are shown in Fig. 5, leading to a reduction in dimensions with significantly improved surface quality for the post-EP specimens.

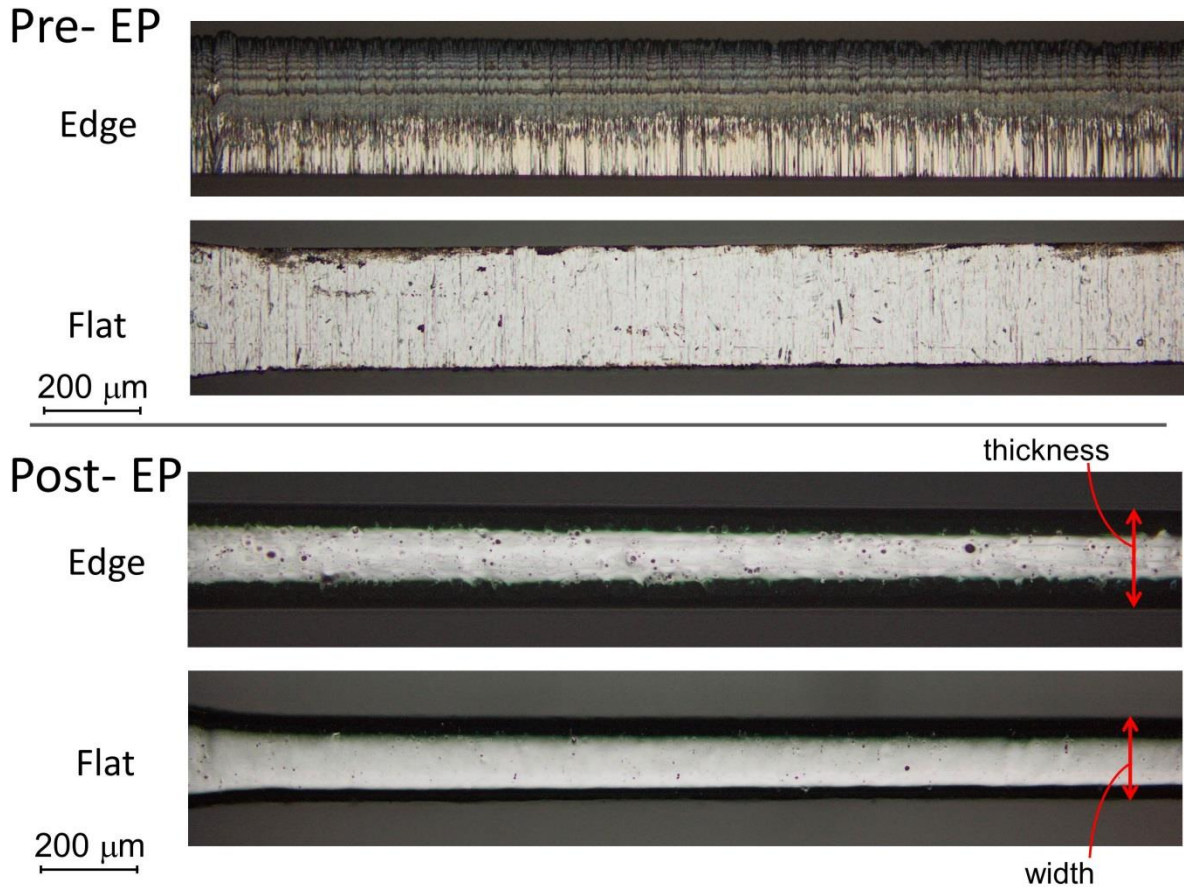


**Figure 5** Optical images comparing surface quality before and after electro-polishing.

After cleaning, the gauge cross-section dimensions of each specimen were measured using an optical microscope; a total of twelve measurements each for width and thickness were recorded, including six measurements along each face of the gauge region (i.e. two flat faces and two edge faces). The average measurements and standard deviations for the gauge cross-section dimensions of twelve specimens are provided in Table 1; average width (flat dimension) and thickness (edge dimension) of 176 and 208  $\mu\text{m}$ , respectively, were recorded. The ranges in measurements for individual specimen width and thickness dimensions were 18.9 and 14.7  $\mu\text{m}$ , respectively.

**Table 1** Final average gauge cross-sectional dimensions for foil dogbone specimens. Standard deviations (SD) are provided for each measurement.

Specimen	Width ( $\mu\text{m}$ )		Thickness ( $\mu\text{m}$ )	
	Average	SD	Average	SD
1	183.18	11.63	221.71	3.48
2	181.12	2.56	213.82	3.86
3	171.43	7.45	205.78	4.64
4	152.43	7.82	179.65	5.86
5	178.00	5.97	203.88	2.82
6	171.44	3.84	212.85	6.83
7	181.12	10.50	220.47	2.86
8	165.36	5.97	197.97	5.98
9	181.46	5.02	210.62	4.71
10	190.56	9.07	209.97	5.17
11	170.61	5.65	208.74	4.70
12	156.49	4.31	189.09	6.21

### 2.3. HCF Testing

HCF testing of the final polished specimens was carried out on the Bose Corporation EnduraTEC® ElectroForce® 3200 Series fatigue tester. The tests were load-controlled at a cyclic nominal stress ratio of  $R_\sigma = \sigma_{max}/\sigma_{min} = 0.1$  for three stress ranges corresponding to maximum stresses of 600, 650 and 700 MPa, where the stress levels were chosen to give an estimated range of lives below  $10^7$  cycles, based on L605 HCF data in Marrey et al. [6]. The tests included a ramp to maximum load, followed by sinusoidal cyclic loading at 1 Hz for 10 cycles, 20 Hz for 1000 cycles and, finally, 50 Hz for the remainder of the test, where the lower initial frequencies are applied to overcome transient feedback control effects. An upper limit or run-out life of  $10^7$  cycles was selected for these tests. Twelve specimens were

successfully tested, comprising four at each stress range, where the loading applied was specific to each specimen, based on the measured gauge cross-section dimensions (i.e. the load was set to achieve the correct stress using the specimen specific dimensions of Table 1).

### **3. Computational Framework**

The finite element computational framework developed for the simulation of the micro-specimen HCF experiments is described in this section, including (i) constitutive models, (ii) representative FE geometries and (iii) microstructure-sensitive indicator parameters for prediction of FCI.

#### ***3.1. Constitutive Models***

Crystal plasticity (CP) modelling is used to define the constitutive behaviour of the foil micro-specimens, describing crystallographic slip on individual slip systems in discrete microstructural grains. Previous studies by the authors on LCF of the L605 alloy have developed both a phenomenological power-law (PL) CP formulation [10] and a physically-based strain-gradient (SG) CP formulation [28]. Both formulations are implemented in this study for comparative assessment of the prediction of the foil HCF behaviour. A brief overview of the key equations is provided here; however further details can be found in the previous work by the authors [10,28].

The PL CP formulation has been implemented in a user-defined material subroutine (UMAT) in Abaqus/Standard by Huang [35] and was later modified by the authors [9] to include kinematic hardening. The visco-plastic PL flow rule, defining the relationship between slip rate on a slip system  $\alpha$ ,  $\dot{\gamma}^\alpha$ , and the slip system resolved shear stress  $\tau^\alpha$ , is given by:

$$\dot{\gamma}^{\alpha} = \dot{a} \operatorname{sgn}(\tau^{\alpha} - x^{\alpha}) \left\{ \left| \frac{\tau^{\alpha} - x^{\alpha}}{g^{\alpha}} \right| \right\}^n \quad (1)$$

where  $\dot{a}$  is a reference strain rate,  $n$  is a rate sensitivity exponent and  $g^{\alpha}$  is the slip system strain hardness. The slip system hardening function in Eq. (1) is based on that of Asaro and co-workers [36–39], for which the evolution is defined as:

$$\dot{g}^{\alpha} = \sum_{\beta} h^{\alpha\beta} \dot{\gamma}^{\beta} \quad (2)$$

where  $h^{\alpha\beta}$  represents self ( $\beta=\alpha$ ) and latent ( $\beta\neq\alpha$ ) hardening moduli, which are given by:

$$h^{\alpha\alpha} = h^{\alpha\beta} = h(\gamma^{\alpha}) = h_0 \operatorname{sech}^2 \left| \frac{h_0 \gamma_a}{g_{\infty} - g_0} \right| \quad (3)$$

where  $h_0$  is the initial hardening modulus,  $g_0$  is equal to the critical resolved shear stress,  $g_{\infty}$  is the saturation stress and  $\gamma_a$  is the accumulated plastic slip. The accumulated plastic slip, used in Eq. (3), is given by:

$$\gamma_a = \sum_{\alpha} \int_0^t |\dot{\gamma}^{\alpha}| dt \quad (4)$$

It was found in previous work, via comparison against uniaxial monotonic and LCF tests, that two kinematic back-stresses are required for accurate simulation of the measured cyclic and tensile behaviour for the L605 alloy [10]. Thus, the total back-stress here, for the flow rule of Eq. (1), is given by:

$$x^{\alpha} = x_1^{\alpha} + x_2^{\alpha} \quad (5)$$

where the Armstrong-Frederick rule for non-linear kinematic hardening is used to describe the evolution of individual back-stresses:

$$\dot{x}_i^\alpha = C_i \dot{\gamma}^\alpha - D_i x_i^\alpha |\dot{\gamma}^\alpha| \quad (6)$$

where  $C_i$  and  $D_i$  are material constants controlling the initial hardening modulus and the rate of decay, respectively. A more complete description of the PL formulation used here is provided in previous work [10]. The calibrated PL CP constants, identified via comparison of the model stress-strain response with cyclic hysteresis loops from LCF tests and tensile curve for the as-received L605 material, are provided in Table 2.

**Table 2** Calibrated PL CP constants for the L605 alloy [10].

$g_0$	100 MPa
$g_\infty$	130 MPa
$h_0$	100 MPa
$C_1$	80 GPa
$D_1$	750
$C_2$	1.25 GPa
$D_2$	0.001
$\dot{a}$	0.002 s <sup>-1</sup>
$n$	50

The physically-based SG CP formulation has been implemented in a user-element subroutine (UEL) in Abaqus/Standard [40] and has been applied by the authors to successfully predict the experimentally-observed grain size effect in LCF behaviour of the L605 alloy [28]. The SG formulation describes the slip due to the glide of statistically-stored mobile dislocations,  $\rho_{SSD,m}$ , through the crystal lattice, where hardening occurs due to the presence of immobile dislocations, including both immobile statistically-stored dislocations,  $\rho_{SSD,i}$ , and geometrically necessary dislocations,  $\rho_{GND}$ . The flow rule for the SG model is defined as:

$$\dot{\gamma}^\alpha = \rho_{SSD,m} b^2 v \exp\left(-\frac{\Delta H}{kT}\right) \sinh \frac{(\tau^\alpha - \tau_c) \gamma_0 b^2}{kT \sqrt{\sum_\alpha (\rho_{SSD,i}^\alpha + \rho_{GND}^\alpha)}} \quad (7)$$



where  $b$  is Burger's vector magnitude,  $\nu$  is the frequency of attempts by mobile dislocations to overcome energy barriers,  $\Delta H$  is the Helmholtz free energy,  $k$  is the Boltzmann constant,  $T$  is the temperature,  $\tau_c$  is the critical resolved shear stress and  $\gamma_0$  is a reference strain. The geometrically necessary dislocation density is defined as a function of the elastic deformation gradient,  $\mathbf{F}^e$ :

$$\sum_{\alpha} (\mathbf{b}^{\alpha} \otimes \boldsymbol{\rho}_{GND}^{\alpha}) = (\text{curl} \mathbf{F}^e)^T \quad (8)$$

where  $\mathbf{b}^{\alpha}$  is Burger's vector and  $\boldsymbol{\rho}_{GND}^{\alpha}$  is comprised of both edge and screw dislocation density components. From Eq. (8), it is clear that the geometrically necessary dislocations form due to spatial gradients in the deformation gradient, thus introducing a strain gradient effect into the formulation. Evolution of the immobile statistically-stored dislocations is given by:

$$\dot{\rho}_{SSD,i}^{\alpha} = \frac{|\dot{\gamma}^{\alpha}|}{b} \left[ \sum_{\alpha} (H^{\alpha\beta} \rho_{SSD,i}^{\alpha} + H^{\alpha\beta} \rho_{GND}^{\alpha}) - 2cy_c \rho_{SSD,i}^{\alpha} \right] \quad (9)$$

where  $H^{\alpha\beta}$  are interaction coefficients describing the mutual immobilisation between dislocations of different slip systems,  $c$  is a constant and  $y_c$  is the critical annihilation distance. The calibrated SG CP constants, identified via comparison of the model stress-strain response with cyclic hysteresis loops from LCF tests for the as-received L605 material, are provided in Table 3; use of the same set of constants also allows the capture of the cyclic plasticity behaviour of heat-treated, coarse grain L605 material [28].

**Table 3** Calibrated SG CP constants for the L605 alloy [28].

$k$	$1.381 \times 10^{-23} \text{ JK}^{-1}$
$T$	293 K
$b$	$2.56 \times 10^{-10} \text{ m}$
$\nu$	$1.0 \times 10^{11} \text{ s}^{-1}$
$\rho_{SSD,0}^{\alpha}$	$5 \times 10^{10} \text{ m}^{-2}$
$\tau_c$	173.5 MPa

$\gamma_0$	$1.0 \times 10^{-3}$
$y_c$	$2. \times 10^{-9} \text{ m}$
$c$	0.01
$\Delta H$	$2.85 \times 10^{-20} \text{ J}$

The L605 alloy has a face centred cubic crystal structure. Therefore, twelve  $\{111\}\langle 110 \rangle$  slip systems are modelled in both CP formulations and anisotropic elasticity, corresponding to the cubic elastic constants given in [10], is employed.

### 3.2. Polycrystal Generation

FE polycrystal geometries are generated for simulation of the foil fatigue testing using a similar approach to that adopted by the authors in [10,28]. In this study, a repeating unit in the foil specimen gauge region is modelled. It is important to emphasise that due to the small cross-sectional area of the specimen, the full cross-section is modelled here, as shown in Fig. 6. A boundary condition assumption has, therefore, only to be made for two unit cell (top and bottom) surfaces. Average width and thickness dimensions reported in the previous section and a dimension of 200  $\mu\text{m}$  in the loading direction are used for the unit cell, as shown in Fig. 7. Abaqus was used to generate a voxel mesh and a Matlab program was employed to superimpose 3D Voronoi tessellations on the mesh and, thus, identify element sets corresponding to grains. A grain volume distribution was generated from the measured grain area statistics of the foil material, shown in Fig. 1(b), whereby approximation of 2D and 3D grains as hexagons and rhombic-dodecahedrons, respectively, with a common dimension  $d$ , allows conversion of each grain area measurement for the foil to a grain volume, as outlined in previous work [10,28]. Five polycrystal morphologies corresponding to grain volume distributions resembling that of the foil were identified, shown in Fig. 7 (labelled as Realizations 1 to 5, respectively).

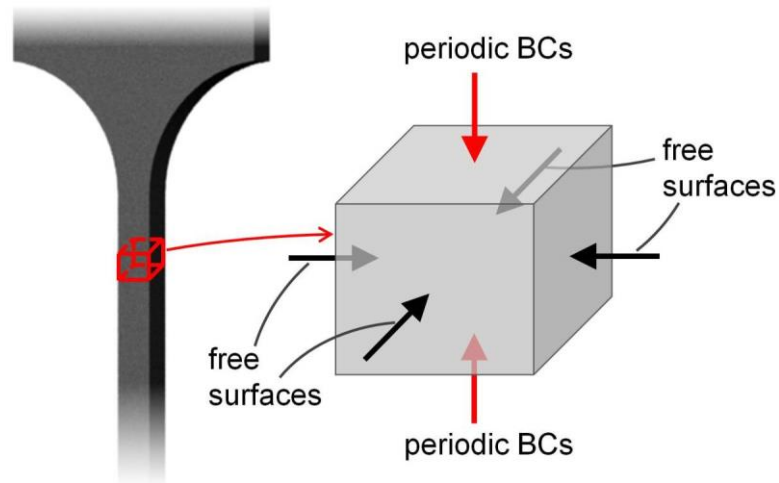


**Figure 6** Schematic of the repeating unit cell modelled for the foil specimen and the boundary conditions applied to the FE model, including two surfaces to which periodic boundary conditions (BCs) are applied, to simulate periodicity along the gauge length, and four free surfaces.

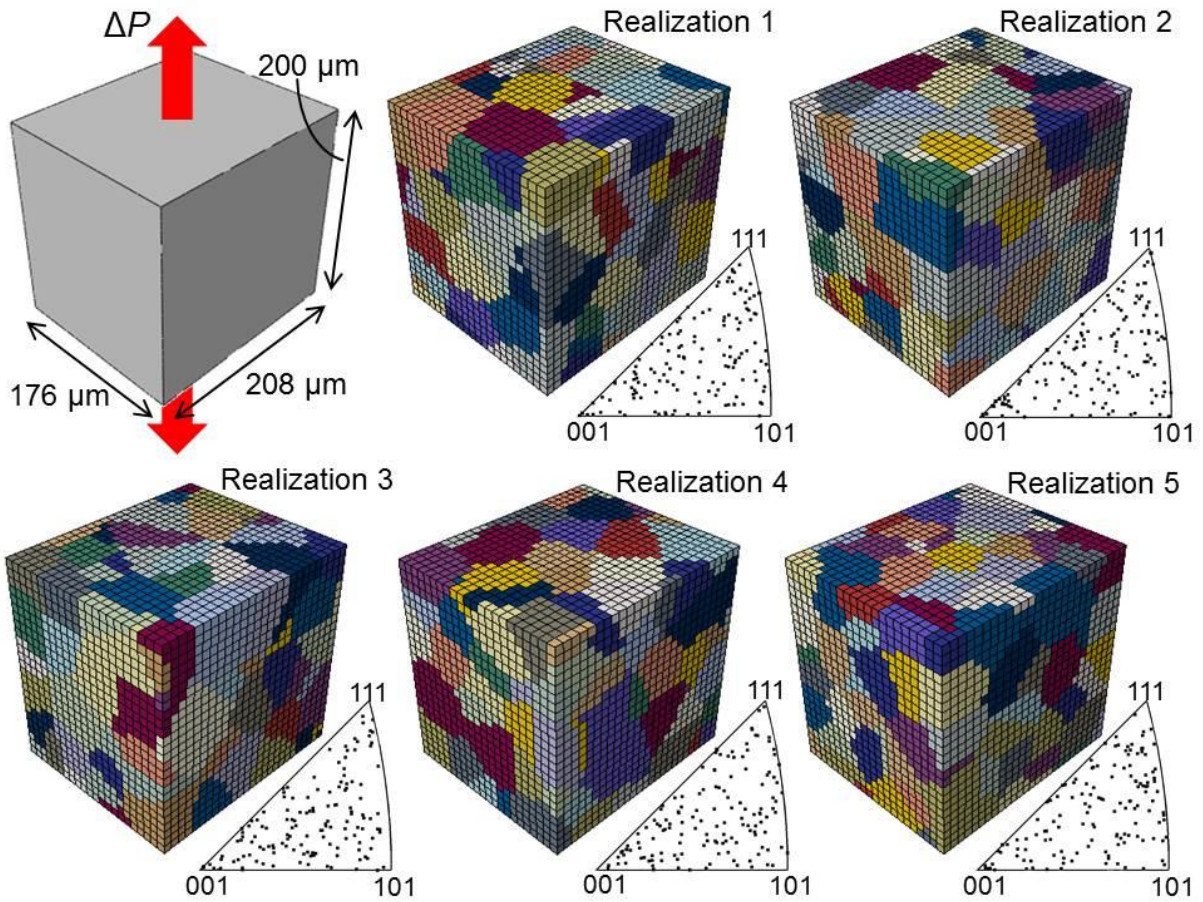


**Figure 7** HCF model dimensions and generated polycrystal realizations, including inverse pole figures indicating crystallographic orientations for grains in each realization.

In order to include precipitates in the models, as described by the authors in [10], random elements were replaced by a seven-element unit, consisting of a precipitate element surrounded by six matrix elements. The approximation of the precipitate shape as a circle in 2D and a sphere in 3D allows conversion of area data to volume data. An average precipitate volume is thus identified and used to determine dimensions of the precipitate element at the centre of the seven-element unit. A sufficient number of regular elements are then replaced by the unit to achieve the experimentally-measured precipitate volume fraction. The precipitates are assumed to be tungsten carbides, based on the EDX observations of Section 2.1, and are thus modelled as hard particles with a Young's modulus of 714 GPa [41]. Each polycrystal model contains 19634 reduced-integration, 20-noded, brick elements,

corresponding to the same mesh density used for in previous 3D polycrystal models for calibration of the CP constitutive formulations [10,28], and between 138 to 140 grains. Random crystallographic orientations are assigned, in keeping with the absence of crystallographic texture observed in Fig. 2, as evident from the inverse pole figures given for each polycrystal in Fig. 7. As the polycrystal models include the full gauge cross-section, periodic displacement boundary conditions are applied on faces perpendicular to the direction of loading only, leaving the remaining four faces unconstrained, representing free surfaces, as illustrated in Fig. 6.

All five polycrystal realizations of Fig. 7 are simulated at each stress range applied in the experiments for the PL CP constitutive model. Due to the computational expense associated with SG CP modelling, only the first realization of Fig. 7 is simulated across the three stress ranges for the SG constitutive model. As for the experimental tests, the fatigue simulations are load-controlled, whereby load levels corresponding to the desired nominal stress levels are applied. The model is initially ramped up to the maximum load level, after which twenty cycles of loading between maximum and minimum load levels are applied.

### **3.3. HCF Predictions**

A key objective of the current study is to investigate the predictive ability of microstructure-sensitive FIPs for fatigue performance under different regimes of loading. Two FIPs are employed in this study. The first is an effective crystallographic plastic strain parameter [25],  $p$ , given as a function of the plastic velocity gradient,  $L^P$ :

$$\dot{p} = \left( \frac{2}{3} L^P : L^P \right)^{1/2} ; \quad p = \int_0^t \dot{p} dt \quad (10)$$

where the plastic velocity gradient can be found by Schmid's Law:

$$L^p = \dot{F}^p \cdot F^{p-1} = \sum_{\alpha} \dot{\gamma}^{\alpha} s^{\alpha} m^{\alpha T} \quad (11)$$

where  $s^{\alpha}$  and  $m^{\alpha}$  are the slip direction and slip plane normal, respectively, on slip system  $\alpha$ . This FIP has been successfully used to predict the number of cycles to FCI across LCF and HCF regimes for a nickel base alloy [25]. Another study established the usefulness of  $p$  for predicting the experimentally-observed FCI sites for explicit ferritic steel microstructures under four-point bending fatigue [24]. The second FIP used is a crystallographic work parameter [26],  $W$ , which sums strain energy dissipation over all slip systems:

$$W = \sum_{\alpha} \int_0^t \tau^{\alpha} \dot{\gamma}^{\alpha} dt \quad (12)$$

The effective plastic strain and crystallographic work FIPs, based on the accumulation of irreversible slip and energy dissipated due to slip, respectively, can be postulated to capture local dislocation activity leading to FCI, as described in the Section 1. Wan et al. [42] postulated that it is the energy stored in the formation of dislocation structures, instead of the energy dissipated, that should be used in predictions of FCI. However, the stored energy criterion presented was calculated as a fraction of the dissipated energy, where the ratio of stored to dissipated energy was assumed to reach a stabilised value after the first few cycles of loading; this is supported by experimental evidence that dissipated energy reaches a given fraction of total energy (composed of dissipated and stored energy) after stabilisation of material cyclic behaviour [43,44]. Based on this assumption, values of stored and dissipated energy (both cyclic and critical quantities) are directly proportional, related by a constant, i.e. the two energy criteria will give the same predictions of  $N_f$ . Thus, the stored energy criterion of Wan et al. [42] is also captured by the crystallographic work parameter,  $W$ , used here.

FCI is predicted to occur when critical values of the cumulative FIPs are reached, i.e.  $p_{crit}$  and  $W_{crit}$ . Maximum cyclic values of the FIPs,  $p_{cyc}$  and  $W_{cyc}$ , extracted from the final cycle of CP simulations can be used to predict the number of cycles to FCI via the relation  $N_i = p_{crit}/p_{cyc}$  (similar for  $W$ ), where  $p_{crit}$  and  $W_{crit}$  are identified via calibration against experimental FCI data. Both local and non-local forms of the FIPs are investigated in this study for prediction of HCF FCI behaviour. The local FIP approach utilises maximum cyclic FIPs at discrete material (integration) points. In contrast to this, the non-local approach uses maximum cyclic FIP values which have been volume averaged over individual grains. Przybyla and McDowell [22,23] also employ grain volume averaging for FIPs in CP polycrystal models to generate probability functions for the occurrence of extreme FIP values, thought to be drivers of FCI. It can be postulated that the FIP distribution over an entire grain contributes to the probability of slip band formation and, thus, FCI in that grain.

Critical values of the local FIPs,  $p_{crit}$  and  $W_{crit}$ , have been identified in previous studies for the PL and SG models ([10] and [28], respectively) via comparison of local maximum cyclic parameters with L605  $N_i$  data extracted from LCF tests, and these are listed in Table 4. For the non-local approach, grain-averaging is applied here to the results of PL and SG simulations presented in [10] and [28], respectively, to generate non-local  $p_{cyc}$  and  $W_{cyc}$  values. The maximum non-local cyclic FIPs are then identified and used to calibrate non-local values of  $p_{crit}$  and  $W_{crit}$  for the two CP models according to the relation  $p_{crit} = N_i p_{cyc}$  (similar for  $W_{crit}$ ), where  $N_i$  is the experimental number of cycles to crack initiation, back-calculated from LCF life data using experimental damage curves, as presented in previous studies [10,28]. The identified non-local critical FIP values, based on grain-averaged data, are provided in Table 4 and the plots in Fig. 8 compare experimental LCF  $N_i$  data with

predictions based on non-local critical FIPs, for the PL and SG models. PL predictions are compared with LCF data of the as-received material in Fig. 8(a), while SG  $p_{crit}$  and  $W_{crit}$  predictions are compared in Figs. 8 (b) and (c), respectively, with LCF data for both as-received ( $d = 32 \mu\text{m}$ ) and heat-treated ( $d = 243 \mu\text{m}$ ) L605 material; both CP constitutive models were calibrated against cyclic data for the as-received material in previous work [10,28]. Calibration of critical FIP values is carried out for both models against one data point, corresponding to the as-received material LCF test at  $\pm 1\%$  total strain, while simulation points corresponding to all other tests are predictions of the experimental data, based on the identified critical FIP values.

**Table 4** Local and non-local critical values of  $W$  and  $p$  for the power-law and strain-gradient CP formulations, identified using cyclic FIP values at discrete material points and volume-averaged over individual grains, respectively.

	<b>Power-Law CP</b>		<b>Strain-Gradient CP</b>	
	$p_{crit}$	$W_{crit}$ (MJ/m <sup>3</sup> )	$p_{crit}$	$W_{crit}$ (MJ/m <sup>3</sup> )
<b>Local (discrete)</b> [10,28]	439.9	$15.63 \times 10^4$	164.3	$9.19 \times 10^4$
<b>Non-local (averaged)</b>	200.8	$7.32 \times 10^4$	123.8	$6.39 \times 10^4$



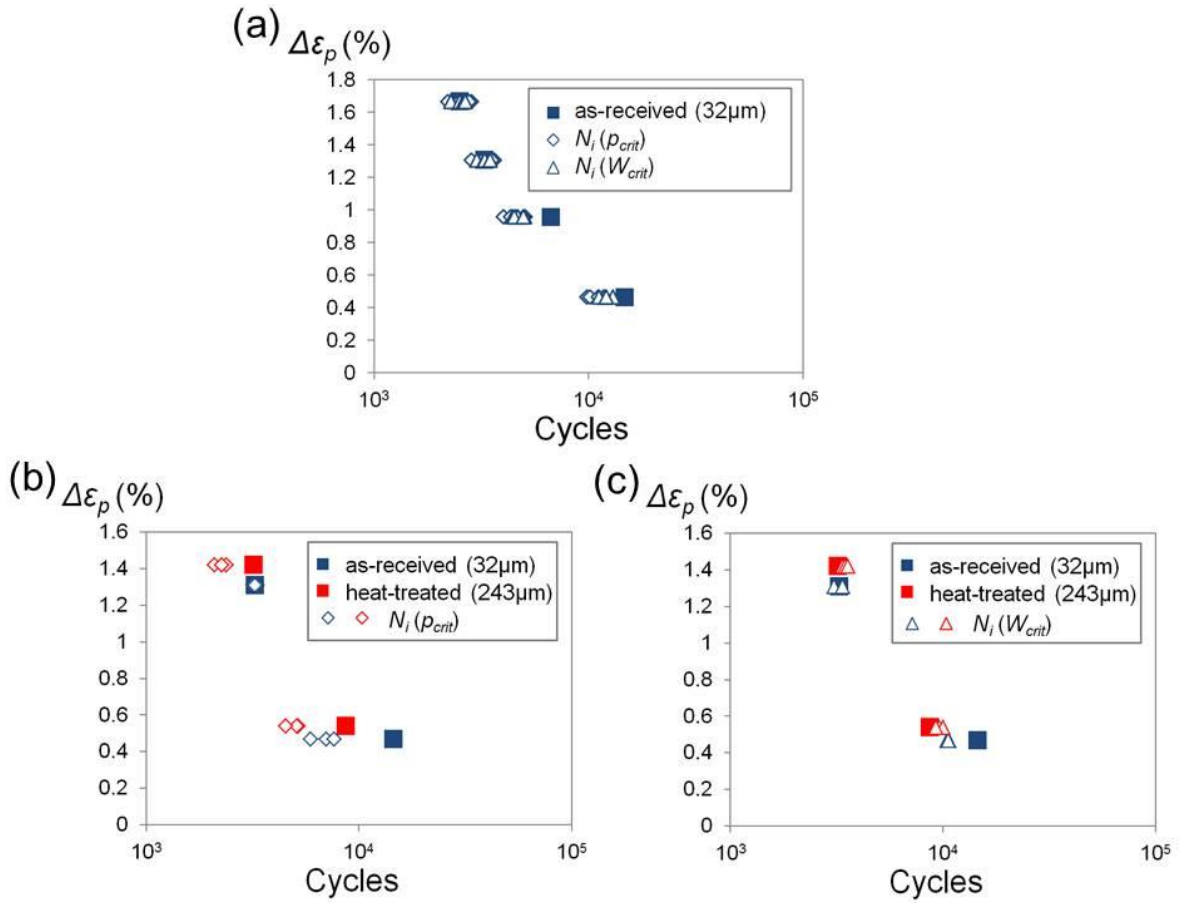


**Figure 8** Comparison of experimental  $N_i$  data for LCF of the L605 alloy with predictions using non-local FIPs (a)  $p_{crit}$  and  $W_{crit}$  for the PL constitutive model, and (b)  $p_{crit}$  and (c)  $W_{crit}$  for the SG constitutive model.

While the local and non-local critical FIP values have been calibrated against LCF data, these FIPs are used here for prediction of HCF behaviour based on the hypothesis that critical FIP values correspond to FCI across both the LCF and HCF regimes, as demonstrated in Manonukul and Dunne [25].

## 4. Results

### 4.1. HCF Tests

Stress-life data for the foil HCF tests is provided in Fig. 9, where a single run-out occurred at the lowest stress range. The Basquin-Goodman relation, derived in previous work [9] for the prediction of HCF total life in the presence of a mean stress,  $\sigma_m$ , is given by:

$$N_f = \left[ \frac{\Delta\sigma}{C_2 \left(1 - \frac{\sigma_m}{\sigma_{TS}}\right)} \right]^{-\gamma_2} \quad (13)$$

where  $\sigma_{TS}$  is the ultimate tensile strength, identified in previously [10] as 1075 MPa for the L605 alloy, and  $C_2$  and  $\gamma_2$  are constants. This relation is recast here to reflect a constant cyclic

and loading ratio  $R_\sigma = \frac{\sigma_{\min}}{\sigma_{\max}} = \frac{\sigma_m - \Delta\sigma/2}{\sigma_m + \Delta\sigma/2}$  :

$$N_f = \left[ \frac{\Delta\sigma}{C_2 \left(1 - \frac{\Delta\sigma(1 + R_\sigma)}{2\sigma_{TS}(1 - R_\sigma)}\right)} \right]^{-\gamma_2} \quad (14)$$

A fit of Eq. (14) to the experimental data is shown in Fig. 9, where  $C_2$  and  $\gamma_2$  are identified as 2351 MPa and 12.09, respectively.

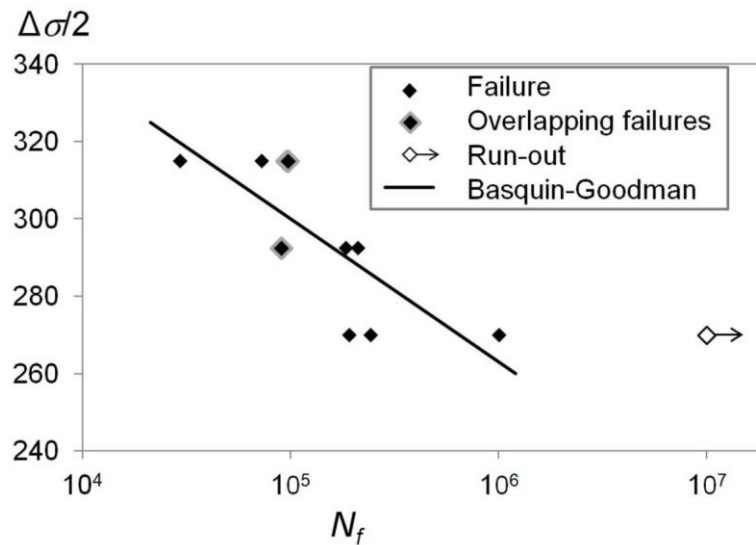


**Figure 9** Stress-life data for HCF tests. A separate marker is used where two data points overlap.

The displacement histories recorded for each test are provided in Fig. 10 (a) and the load-displacement hysteresis loops output from the EnduraTEC® ElectroForce® fatigue tester for one specimen at each stress range are given in Fig. 10 (b). Ratcheting occurs during the first portion of each test, due to the stress-controlled cyclic plastic deformation with tensile mean stress, gradually followed by a plateau corresponding to elastic shakedown. The tests for which fracture occurred (all except Specimen 1) were characterised by a rapid increase in displacement at the end of the test, attributed to the loss of stiffness in the specimen due to accentuation and localisation of fatigue damage and failure, indicating that  $N_i \approx N_f$ . The hysteresis loops show a similar trend, whereby the loops for the highest stress level (Fig. 10(b),  $\sigma_{max} = 700$  MPa) appear marginally wider.

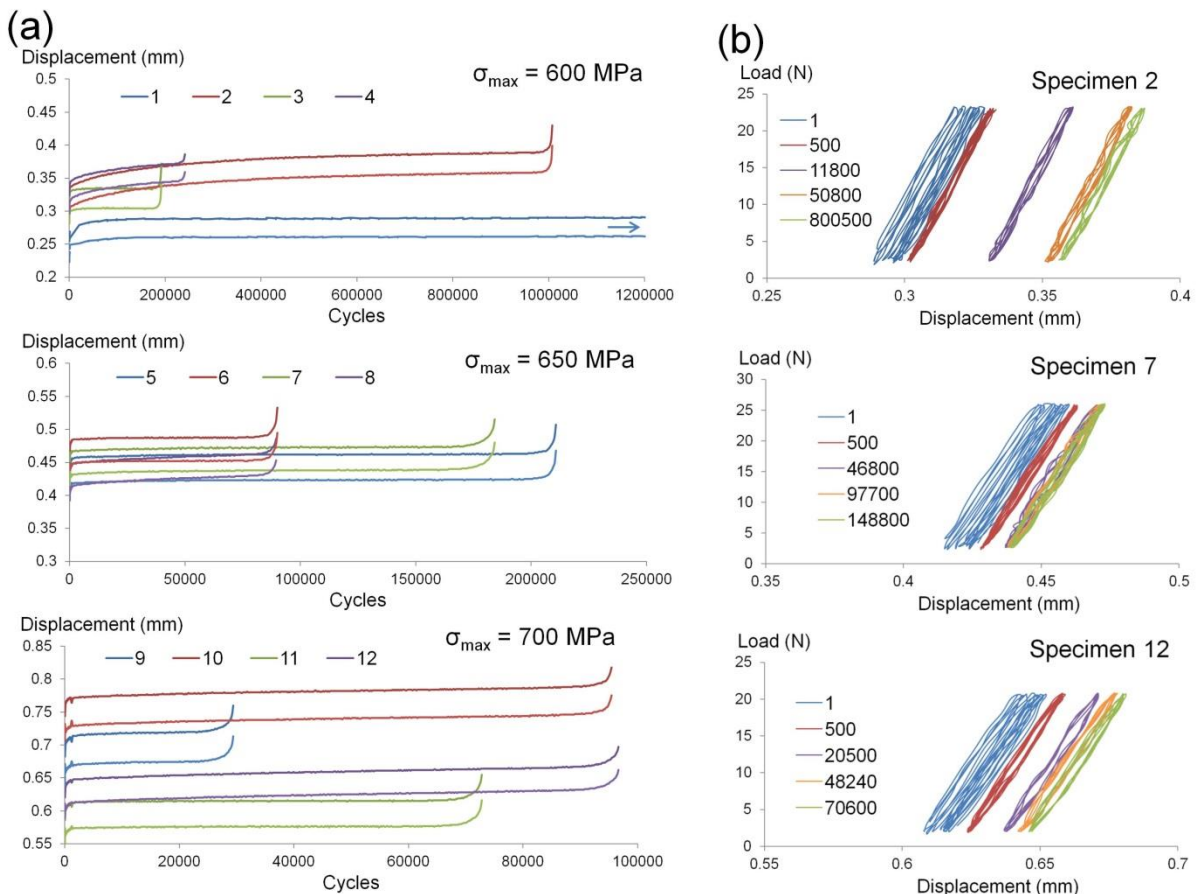


**Figure 10** (a) Displacement histories for each specimen, divided according to maximum nominal stress and (b) sample load-displacement hysteresis loops for one specimen from each stress range, where ten cycles of loading are shown at each cycle number.

Post-test optical images of each specimen are provided in Fig. 11. The fracture region is shown for each specimen, with the exception of the run-out specimen (1) for which a portion of the gauge region is shown. Specimens 5, 6 and 9 show fractures which are located close to the fillet at the end of the gauge length, while all other fractures occur within the gauge length. Surface roughening is visible for every specimen, and this roughening appears to increase with stress range. Slip lines are seen clearly in a magnified view of Specimen 9 in Fig. 11, for example, at the highest stress range.

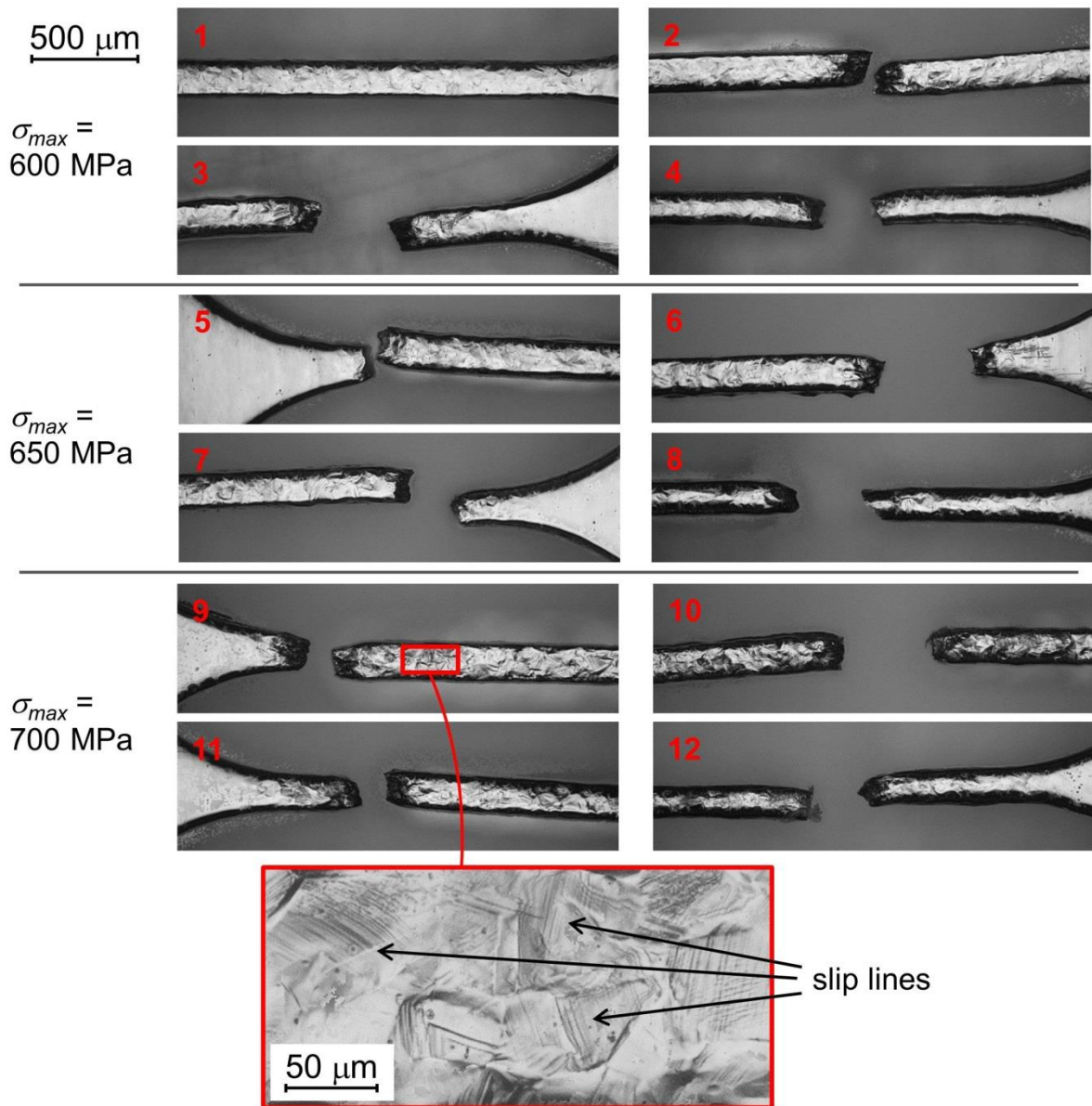


**Figure 11** Optical images of specimens after fatigue tests, including a magnified view of a region near the fracture site for one specimen.

#### 4.2. HCF Simulations

In order to predict life via the local FIP approach, local  $p_{cyc}$  and  $W_{cyc}$  values are extracted from the final cycle of loading in the HCF simulations for each material integration point and the maximum local cyclic FIPs are identified. The number of cycles to crack initiation is then predicted via the relation  $N_i = p_{crit}/p_{cyc}$  (similar for  $W$ ), using previously identified local  $p_{crit}$  and  $W_{crit}$  values (Table 4). The results are shown in Fig. 12, compared to the measured life

data. The  $N_i$  predictions from the PL model (blue markers) generally lie within the range of the experimental life data. However, for the SG models (red markers), life is generally under-predicted, particularly for  $W_{crit}$ , for which the predictions are lower than the experimental data by approximately one order of magnitude.

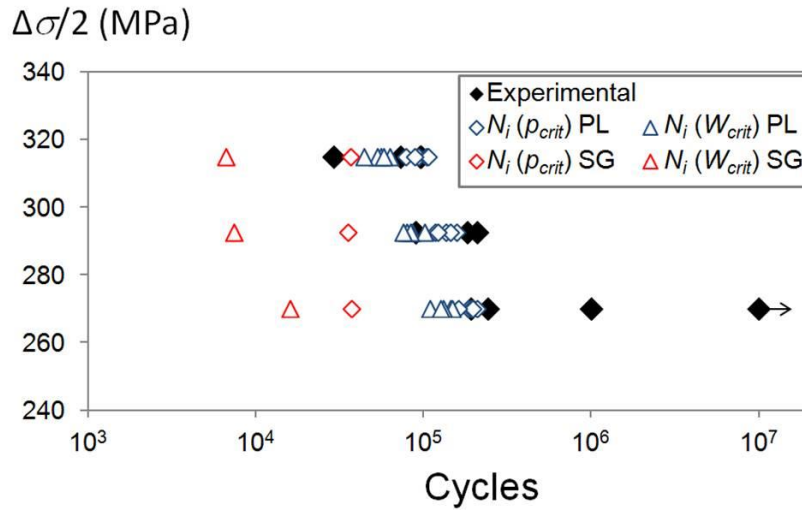


**Figure 12** Comparison of  $N_i$  predictions for the PL and SG models with experimental foil life data using local cyclic FIPs.

Snapshot plots of the final  $p_{cyc}$  and  $W_{cyc}$  distributions for one realization of the PL and SG models are shown in Fig. 13. The peaks in all distributions occur in elements at the free surface. In some cases peaks occur in corner elements, representing a junction between two free surfaces and a third periodically constrained surface. While this is not unrealistic, some of the peaks in corner elements are much higher in comparison with peaks not located in corner elements. Particularly for  $W_{cyc}$  distributions in the SG models, peaks are an order of magnitude higher than expected, as illustrated, for example, in a magnified view for the  $\sigma_{max}=600$  MPa case of Fig. 13, demonstrating a sensitivity of the SG model to the mixed free surface-periodic boundary conditions applied. The low predicted  $N_i$  values for the SG  $W_{crit}$

method of Fig. 12 are attributed to these local peaks in  $W_{crit}$  for the length scale-dependent model.

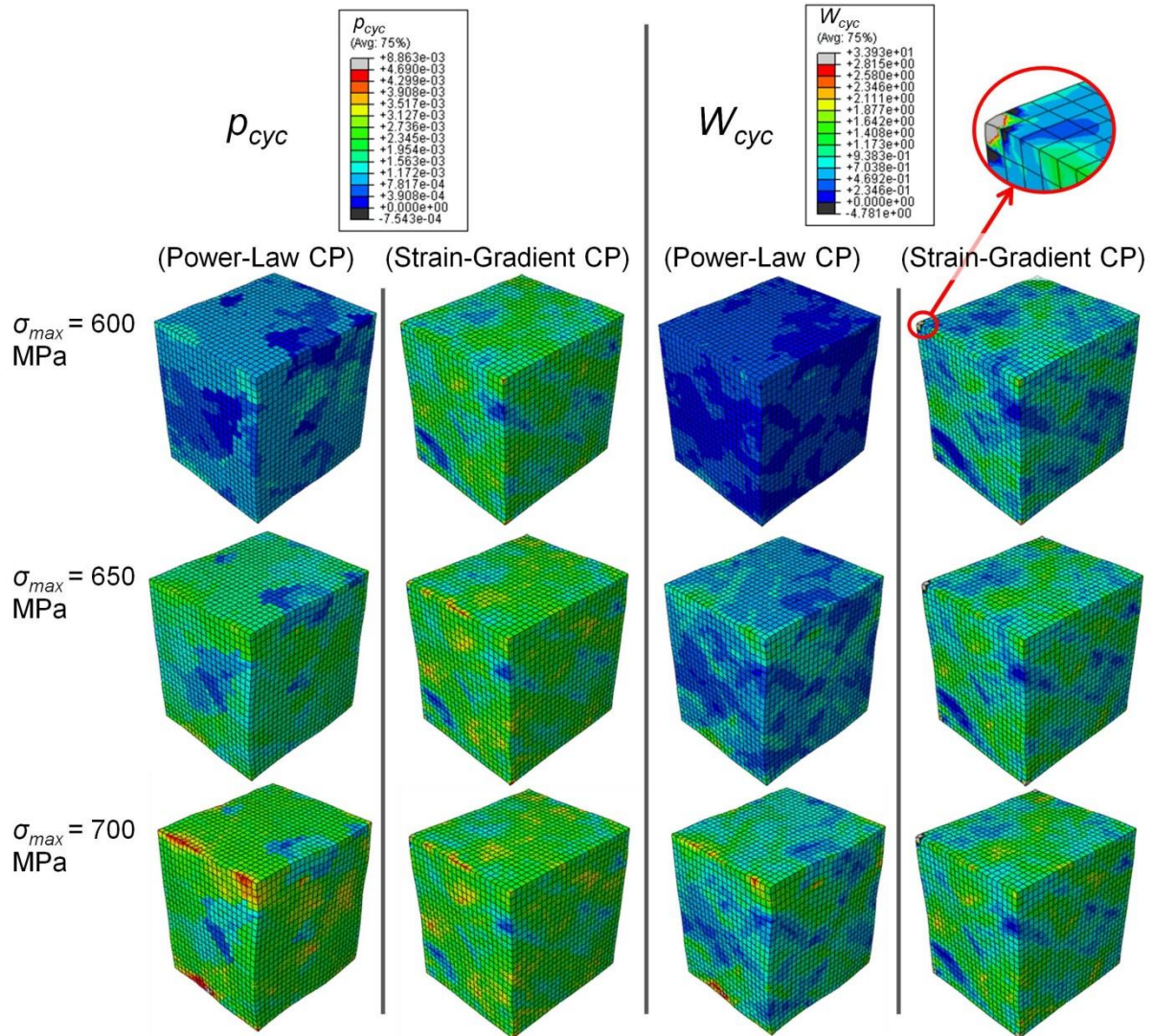


**Figure 13** Distributions of  $p_{cyc}$  and  $W_{cyc}$  for one realization of the PL models and for the SG models.

A non-local, volume-averaging FIP approach is also applied for the prediction of foil FCI behaviour. Similar to the local prediction approach, non-local  $p_{cyc}$  and  $W_{cyc}$  values are extracted for each grain in the HCF simulations. The maximum cyclic FIP values are identified and the newly calibrated non-local  $p_{crit}$  and  $W_{crit}$  values of Table 4 are used for the prediction of  $N_i$ , shown in Fig. 14. SG predictions, again, tend towards lower lives. However,

predictions for the two constitutive models are close, compared with Fig. 12 where discrete FIP values are used. FCI is predicted to occur in grains at the free surface across all stress levels, for both CP formulations; the critical grain is located at a corner for only one PL realization (at  $\sigma_{max}=700$  MPa). The predictions lie within the range of experimental data for the highest stress level, but are seen to decrease somewhat relative to the test data at lower stress levels.

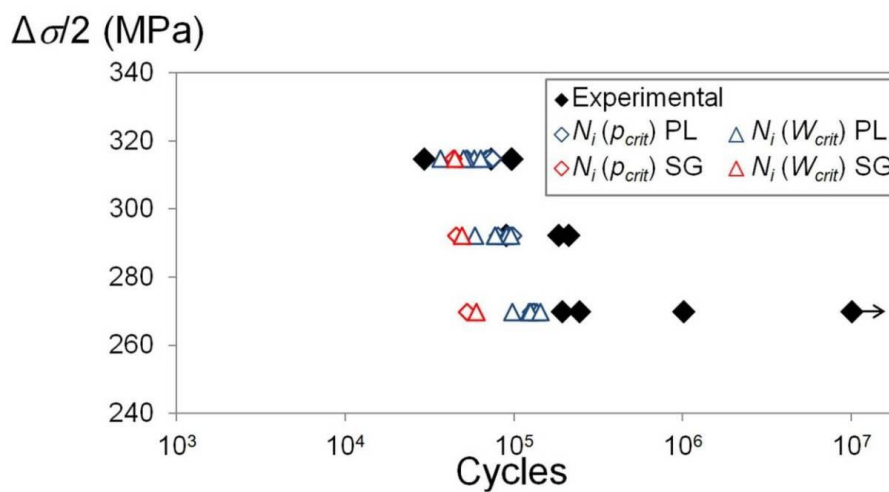


**Figure 14** Comparison of foil HCF data with  $N_i$  predictions using non-local (grain-averaged) FIPs.

## 5. Discussion

### 5.1. HCF Tests

The experimental fatigue data of Fig. 9 shows a clear trend, which follows the Basquin-Goodman relation of Eq. (14), where scatter in data is expected due to the dependence on microstructure inhomogeneity in the HCF loading regime, particularly for micro-scale specimens. The hysteresis loops of Fig. 10 (b) clearly show the elasticity-dominated nature of loading. Ratchetting occurs in the earlier part of tests; however, only a small amount of plasticity is observed in hysteresis loops except, perhaps, for the highest stress range where the area encompassed by loops becomes more discernible, indicating a transition towards



more widespread plasticity. The optical images of Fig. 11 clearly demonstrate the important role of micro-slip in fatigue of the foil specimens. Slip lines are visible in a large number of grains, i.e. grains favourably oriented for slip. Increased surface roughness and improved visibility of slip lines is observed with increasing stress range, due to increased plasticity. Although some fractures occur at the edge of the gauge region (Specimens 5, 6 and 9), the fatigue lives of these specimens are consistent with other specimens for which fractures occur well within the gauge region.

## **5.2. Micromechanical Simulations**

Two different approaches have been presented in Section 4.2 for interpretation of micromechanical simulation results, to predict  $N_i$  for the foil HCF tests. The PL predictions were found to be less sensitive to the model boundary conditions and generally give better correlation with the experimental life data. The local PL  $N_i$  predictions lie in the range of experimental data in Fig. 12; both FIPs perform reasonably well, with  $p_{cyc}$  predicting marginally longer lives in general. For predictions based on non-local cyclic FIP values, shown in Fig. 14, the PL predictions lie at the lower end of the measured life range for the lowest stress level. It can be postulated that as stress range reduces and HCF life increases, microstructural inhomogeneity and local peaks in slip and strain energy dissipation become more influential on FCI. In contrast, for higher stress ranges, the influence of peaks formed in the microstructure diminishes in importance and less-localised or average slip and crystallographic work are adequate predictors of FCI. This is also evident from the effectiveness of grain volume-averaged FIPs in predictions of L605 LCF behaviour for both the PL and SG models in Fig. 8.

Local SG  $N_i$  predictions are more conservative than PL predictions, as seen in Fig. 12, particularly for  $W_{cyc}$ . This can be attributed to peaks in SG  $W_{cyc}$  distributions being an order of magnitude higher than present elsewhere in the model, as seen in Fig. 13. The use of non-local (grain-averaged) FIPs, which is consistent with the nature of the length scale-dependent SG model, diminishes the effect of unexpectedly high peaks in FIP distributions. However, the resulting predictions show low sensitivity to the applied stress ranges.

$N_i$  predictions presented here for both the local and non-local FIPs are based on the assumption of stabilised cyclic FIP values. Examples of the evolution of the maximum local  $p_{cyc}$  and  $W_{cyc}$  for PL and SG models are provided in Fig. 15 (a) and (b), respectively. While the trends indicate that the cyclic FIPs are not fully stabilised, all curves appear to be approaching stabilisation. Thus use of the cyclic FIP values for the final cycle simulated are sufficient for the purposes of this study. Fully stabilised cyclic FIPs would result in a slight increase in life predictions, improving correlation with experimental life data, as seen from Figs. 12 and 14. The non-smooth SG plots of Fig. 15 (b) indicate that the SG model is less stable than the PL model, for the local FIP approach.

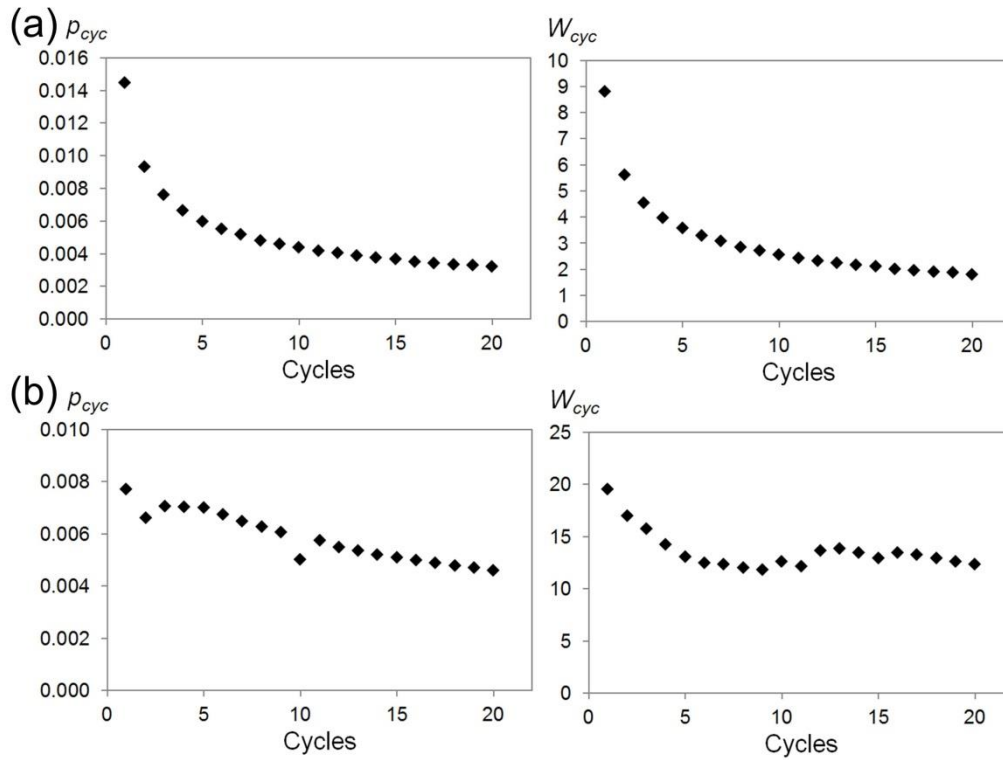


**Figure 15** Evolution of the maximum local FIPs,  $p_{cyc}$  and  $W_{cyc}$  at  $\sigma_{max}=650$  MPa for (a) one realization of the PL model and (b) the SG model.

Recalling [28], the SG formulation has been calibrated via comparison of the macroscopic response of a polycrystal model against LCF data for as-received and heat-treated L605 specimens, with emphasis on capture of the stabilised hysteresis loops, rather than monotonic initial yielding. The PL formulation has been calibrated against both tensile (monotonic) and LCF data for the as-received L605 material, as described in [10], facilitated by the inclusion of back-stress terms in the PL model, providing increased control over hysteresis loop shapes. The PL model in this instance is, thus, better equipped for HCF predictions. The SG model is also shown to be more sensitive to boundary conditions, evident from the peaks in corner elements, and it would likely benefit from further mesh refinement to better capture local strain-gradients away from the corners, at grain boundaries and precipitates. However, the importance of SG effects cannot be ignored, particularly where a change in grain size is

considered. An average grain size of 38  $\mu\text{m}$  is measured here for the L605 foil, which is quite close to the measured average grain size for the as-received L605 material, used in previous studies [10,28] (32  $\mu\text{m}$ ) for the calibration of the two CP formulations. Therefore, use of the PL model is acceptable here. However, for material with a gradient in grain sizes (e.g. at the treated surface of a component), a different distribution of grain sizes or an overall decrease in grain size, as discussed in [28], a significant change of fatigue behaviour for the alloy could result. In such cases, the SG formulation would be a more appropriate constitutive model choice, since it would automatically capture the effect of grain size [28] without the need to re-calibrate; the PL model would need to be separately calibrated for each microstructure with different grain size statistics.

The micromechanical models presented here are less successful at capturing the measured scatter in life data, particularly at lower stresses. In the plot of Fig. 12 the majority of predictions remain in the  $10^4$  and  $10^5$  cycle regimes, whereas, one test specimen failed at about  $10^6$  cycles and another specimen reached the  $10^7$  run-out limit. As expected, use of grain volume-averaged cyclic FIP values reduces further the predicted scatter (Fig. 14). It can be postulated that extreme microstructure combinations (e.g. the “rogue” grain combination modelled in fatigue facet nucleation simulations by Dunne and Rugg [45]) must be modelled in order to capture true scatter. The polycrystal realizations of Fig. 7 represent microstructure samples with grain volume distributions strongly correlated to the average value of grain volume and, therefore, are limited with respect to predicting the influence of microstructural inhomogeneity. Clearly, also, the use of only five polycrystal realizations limits predicted scatter. A study by Przybyla and McDowell [22] show that use of twenty five SVEs is sufficient to investigate the link of potentially influential microstructural attributes with extreme values of FIPs, via probability functions.

Some further observations can be made on preferential sites for FCI in HCF, based on the CP simulations presented here. Aside from the unconstrained free surfaces, predicted FCI sites are also observed to be influenced by precipitates and grain boundaries. The locations of all FCI sites predicted are listed in Table S1 of the supplementary data. Corner element predictions are excluded here, due to sensitivity of corner elements to the applied boundary conditions. The following general trends for FCI locations are observed for the PL models:

- FCI is generally predicted at the free surface, but the probability of subsurface FCI increases with decreasing stress level. This is consistent with previous observations of increasing probability of FCI due to subsurface mechanisms at increased numbers of cycles [15], a trend also predicted by Przybyla et al. [46] for the HCF regime, using extreme value statistics.
- Grain boundaries are dominant predicted locations for FCI, both subsurface and at the free surface. This is corroborated by experimental observations in the literature of FCI occurring in PSBs at the grain boundaries (e.g. Schwartz et al. [47]), which act as barriers to dislocation motion, causing the build-up of dislocations and the formation of dislocation structures.
- FCI is predicted to occur adjacent to precipitates for approximately 50% of  $W_{cyc}$  predictions. Based on a product of shear stress and plastic slip,  $W_{cyc}$  is more sensitive to the influence of increased stresses near precipitates than the purely slip-based  $p_{cyc}$ .
- All subsurface FCI sites are predicted either at a grain boundary or adjacent to a precipitate or both.

For the SG model, FCI sites are predicted to occur at the free surface for  $p_{cyc}$ , but away from grain boundaries and precipitates. This is attributed to increased material hardening and, thus, reduced slip at grain boundaries and precipitates due to build-up of geometrically necessary

dislocations in SG models. In contrast,  $W_{cyc}$  predictions for the SG model forecast subsurface FCI sites, both at grain boundaries and adjacent to precipitates, capturing an increase in crystallographic work at these stress-concentrators. For both the PL and SG models, there are no conclusive trends to show that FCI predictions either subsurface, adjacent to precipitates or at grain boundaries correspond to an increase or decrease in  $N_i$  values, for the study presented here. Twin boundaries observed in the foil microstructure in Figs. 1 (a) and 2 (a) are not represented in the polycrystal models presented here, as for previous macro-scale material studies [10,28]. It is anticipated, based on the study of Castelluccio and McDowell [48] on the effect of twin boundaries on FIP accumulation, that twin boundaries would also be predicted as preferred sites for FCI.

The plots of Figs. 16 (a) and (b) show ranges of maximum Schmid factors across all slip systems with respect to the direction of applied load for all integration points and for all grains, respectively, in each of the micromechanical models. The markers indicate integration points (Fig. 16 (a)) and grains (Fig. 16 (b)) for which FCI is predicted to occur using maximum local and non-local values, respectively, of  $p_{cyc}$  and  $W_{cyc}$ , again excluding predictions at corner elements for local predictions. For the local FIP approach in Fig. 16 (a), maximum Schmid factors at the predicted sites of FCI are generally in the upper half of the full range, with  $W_{crit}$  predictions in particular favouring higher maximum Schmid factors. However, a consistent correlation between Schmid factor and FCI location cannot be made, for predictions based on local FIPs. For the non-local FIP approach, all FCI predictions occur for grains with maximum Schmid factors in the upper half of the range shown (Fig. 16 (b)), indicating a clear correlation between grain Schmid factor and FCI location.

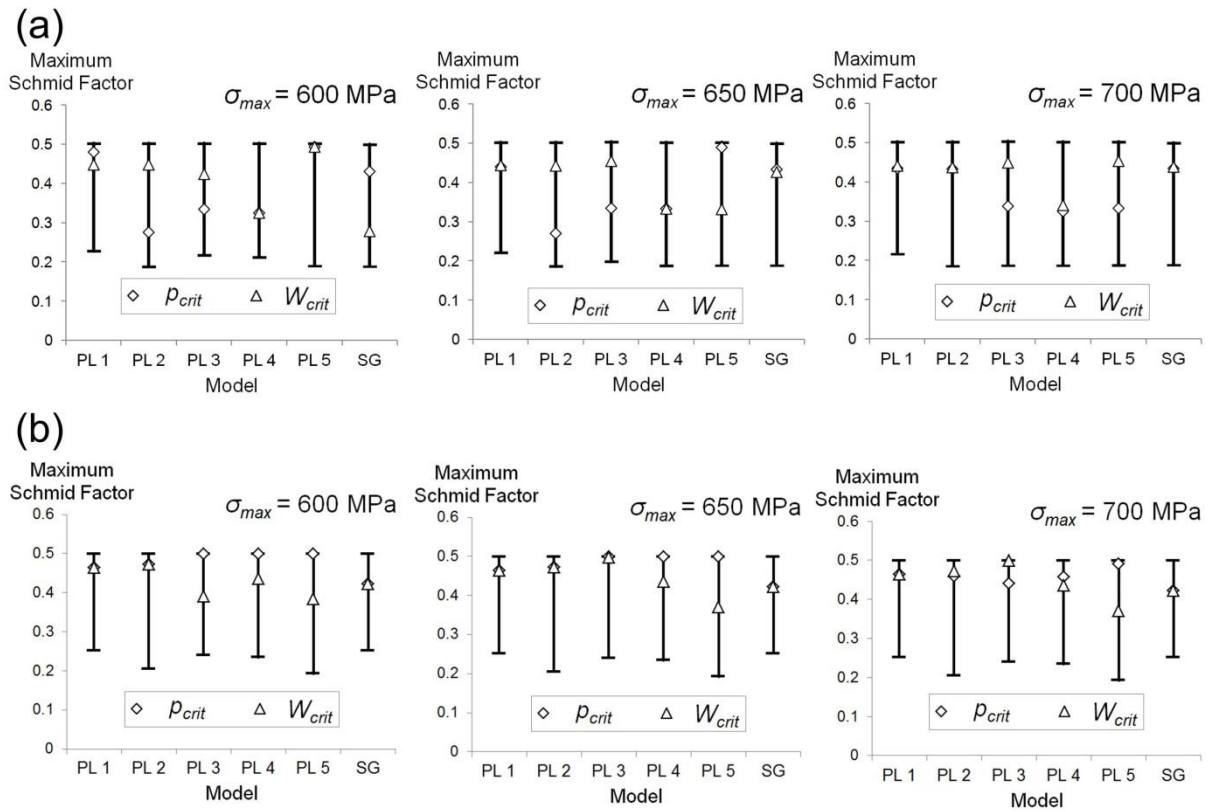


**Figure 16** Maximum Schmid factor at predicted FCI locations using (a) local FIPs at discrete points and (b) non-local (grain-averaged) FIPs. The range of maximum Schmid factors in each model is also shown.

Due to the microstructure-sensitive nature of the tests and models presented, multiaxiality effects in individual grains due to the microstructure itself is inherently accounted for. However, further validation is required to investigate performance of the micromechanical framework as a tool in stent fatigue design. The uniform gauge length of the foil specimens tested here and uniaxial loading applied do not capture the macroscopically multiaxial nature of stent fatigue. Also, as high mean stresses are common in stents, owing to the high deformation installation procedure, further testing at higher cyclic load ratios than that used here would provide further insight into mean stress effects on stent fatigue performance.

It is recommended that future work should focus on the development of experimental methods for identification of the critical values of the FIPs investigated here, to resolve the unavoidable uncertainties inherent in a model-based identification. It is evident from Table 4 that in a model-based process for identification of the FIP material constants (parameters), the identified values naturally depend on the specifics of the microstructure-sensitive, constitutive-failure model combination and associated assumptions (e.g. local, non-local, PL CP, SG CP, etc.). The key message of this paper is that, for a given constitutive-failure model combination (and associated assumptions), it is possible to identify, via LCF test calibration, a critical value of microstructure-sensitive FIP which can successfully predict HCF crack initiation. Naturally, the quality of this prediction depends, to a certain degree, on the quality and consistency of the combination of microstructure representation, constitutive model, failure (FIP) model and associated assumptions. It is postulated that the experimental values for  $p_{crit}$  and  $W_{crit}$  lie within the range of critical FIP values identified (Table 4) for the different constitutive-failure model combinations investigated here. The range of critical FIP values identified (e.g. between 123.8 and 439.9 for  $p_{crit}$ ) would not significantly affect predicted HCF behaviour on a logarithmic life scale and, thus, choice of critical FIP (within this range) does not have a significant effect on predicted correlation with HCF test data, even if consistency is still advised between constitutive-failure model combination used for FIP calibration and for prediction.

The micromechanics approach for the HCF behaviour of CoCr alloy stents presented here addresses for the first time a need, highlighted in a study by Marrey et al. [6], for CoCr stent fatigue predictive modelling capability which accounts for the influence of microstructure. Validation of the predictive ability of the micromechanical framework for HCF behaviour of the L605 CoCr alloy has been presented; previous work demonstrated application of the



framework as a tool for the efficient design of CoCr stents against fatigue. For future development of the micromechanical framework for stent fatigue assessment and design, the results of the current study indicate that the phenomenological PL CP approach performs well and is suitable for use when data on the stent microstructure is available for calibration. However, in the case that variations in the precipitate content, grain size and other attributes affecting strain-gradients exist between calibration and final stent material, it is recommended, based on the work of a previous study [28], that the SG constitutive model be used.

## **6. Conclusions**

The HCF behaviour of the L605 CoCr alloy has been successfully characterised via testing of foil micro-specimens. Slip lines observed on the tested specimens reaffirm the need for microstructure-sensitive prediction techniques for HCF of micro-components. An L605 micromechanical framework for the prediction of this behaviour has been developed, using multiple FE microstructure realizations of the foil specimen cross-section and two CP formulations coupled with microstructure-sensitive FIPs.

Polycrystal simulations allowed identification of free surfaces, precipitates and grain boundaries as preferred sites for FCI, using local FIP predictions, while grain Schmid factor is also shown to have influence on FCI location, using non-local FIP predictions. Predictions of number of cycles to FCI using the power-law CP formulation are in good agreement with experimental data, while coupling of a non-local FIP approach with the strain-gradient, length scale-dependent CP formulation produces generally conservative predictions of the foil life data. Parameters  $p_{crit}$  and  $W_{crit}$ , calibrated against LCF data and previously shown to be

effective across multiple grain sizes, have been validated here as indicators of FCI for the HCF regime also.

The micromechanical framework has been used here to predict the experimental fatigue behaviour of a CoCr foil micro-specimen, representative of stent fatigue both in terms of size-scale and applied HCF loading, and, thus, fulfils the need for a microstructure-sensitive approach to stent fatigue assessment and design.

### **Acknowledgements**

The authors would like to acknowledge funding from the Irish Research Council under the EMBARK Initiative Scheme and the Irish Centre for High-End Computing (ICHEC) for the provision of computational facilities and support. Laser-cutting presented here was carried out at the National Centre for Laser Applications (NCLA) at the National University of Ireland, Galway and EBSD work was carried out at the Materials and Surface Science Institute (MSSI) at the University of Limerick.

### **References**

- [1] D.O. Halwani, P.G. Anderson, B.C. Brott, A.S. Anayiotos, J.E. Lemons, The role of vascular calcification in inducing fatigue and fracture of coronary stents, *J. Biomed. Mater. Res. B Appl. Biomater.* 100B (2012) 292–304. doi:10.1002/jbm.b.31911.
- [2] F. Shaikh, R. Maddikunta, M. Djelmami-Hani, J. Solis, S. Allaqaband, T. Bajwa, Stent fracture, an incidental finding or a significant marker of clinical in-stent restenosis?, *Catheter. Cardiovasc. Interv.* 71 (2008) 614–618. doi:10.1002/ccd.21371.
- [3] G. Sianos, S. Hofma, J.M.R. Ligthart, F. Saia, A. Hoye, P.A. Lemos, et al., Stent fracture and restenosis in the drug-eluting stent era, *Catheter. Cardiovasc. Interv.* 61 (2004) 111–116. doi:10.1002/ccd.10709.
- [4] T. Celik, A. Iyisoy, B. Jata, C.U. Yuksel, E. Isik, Stent fracture: A new villain of the village, *Int. J. Cardiol.* 138 (2010) 100–101. doi:10.1016/j.ijcard.2008.06.010.
- [5] R.N. Nair, K. Quadros, Coronary Stent Fracture A Review of the Literature, *Card. Cath Lab Dir.* 1 (2011) 32–38. doi:10.1177/2150133510395496.
- [6] R.V. Marrey, R. Burgermeister, R.B. Grishaber, R.O. Ritchie, Fatigue and life prediction for cobalt-chromium stents: A fracture mechanics analysis, *Biomaterials.* 27 (2006) 1988–2000. doi:10.1016/j.biomaterials.2005.10.012.

- [7] M.H. El Haddad, T.H. Topper, K.N. Smith, Prediction of non propagating cracks, *Eng. Fract. Mech.* 11 (1979) 573–584. doi:10.1016/0013-7944(79)90081-X.
- [8] O. Barrera, A. Makradi, M. Abbadi, M. Azaouzi, S. Belouettar, On high-cycle fatigue of 316L stents, *Comput. Methods Biomech. Biomed. Engin.* (2012) 1–12. doi:10.1080/10255842.2012.677442.
- [9] C.A. Sweeney, P.E. McHugh, J.P. McGarry, S.B. Leen, Micromechanical methodology for fatigue in cardiovascular stents, *Int. J. Fatigue.* 44 (2012) 202–216. doi:10.1016/j.ijfatigue.2012.04.022.
- [10] C.A. Sweeney, B. O’Brien, P.E. McHugh, S.B. Leen, Experimental characterisation for micromechanical modelling of CoCr stent fatigue, *Biomaterials.* 35 (2014) 36–48. doi:10.1016/j.biomaterials.2013.09.087.
- [11] S. Schievano, A.M. Taylor, C. Capelli, P. Lurz, J. Nordmeyer, F. Migliavacca, et al., Patient specific finite element analysis results in more accurate prediction of stent fractures: application to percutaneous pulmonary valve implantation, *J. Biomech.* 43 (2010) 687–693. doi:16/j.jbiomech.2009.10.024.
- [12] S. Wiersma, F. Dolan, D. Taylor, Fatigue and fracture in materials used for micro-scale biomedical components., *Biomed. Mater. Eng.* 16 (2006) 137–146.
- [13] S. Wiersma, D. Taylor, Fatigue of materials used in microscopic components, *Fatigue Fract. Eng. Mater. Struct.* 28 (2005) 1153–1160. doi:10.1111/j.1460-2695.2005.00952.x.
- [14] A.R. Pelton, V. Schroeder, M.R. Mitchell, X.-Y. Gong, M. Barney, S.W. Robertson, Fatigue and durability of Nitinol stents, *J. Mech. Behav. Biomed. Mater.* 1 (2008) 153–164. doi:16/j.jmbbm.2007.08.001.
- [15] K.S. Chan, Roles of microstructure in fatigue crack initiation, *Int. J. Fatigue.* 32 (2010) 1428–1447. doi:10.1016/j.ijfatigue.2009.10.005.
- [16] D.L. McDowell, F.P.E. Dunne, Microstructure-sensitive computational modeling of fatigue crack formation, *Int. J. Fatigue.* 32 (2010) 1521–1542. doi:10.1016/j.ijfatigue.2010.01.003.
- [17] F.P.E. Dunne, Fatigue crack nucleation: Mechanistic modelling across the length scales, *Curr. Opin. Solid State Mater. Sci.* 18 (2014) 170–179. doi:10.1016/j.cossms.2014.02.005.
- [18] M.D. Sangid, The physics of fatigue crack initiation, *Int. J. Fatigue.* 57 (2013) 58–72. doi:10.1016/j.ijfatigue.2012.10.009.
- [19] M.D. Sangid, H.J. Maier, H. Sehitoglu, The role of grain boundaries on fatigue crack initiation - An energy approach, *Int. J. Plast.* 27 (2011) 801–821. doi:16/j.ijplas.2010.09.009.
- [20] M.D. Sangid, H.J. Maier, H. Sehitoglu, An energy-based microstructure model to account for fatigue scatter in polycrystals, *J. Mech. Phys. Solids.* 59 (2011) 595–609. doi:16/j.jmps.2010.12.014.
- [21] M.D. Sangid, H.J. Maier, H. Sehitoglu, A physically based fatigue model for prediction of crack initiation from persistent slip bands in polycrystals, *Acta Mater.* 59 (2011) 328–341. doi:16/j.actamat.2010.09.036.
- [22] C.P. Przybyla, D.L. McDowell, Microstructure-sensitive extreme value probabilities for high cycle fatigue of Ni-base superalloy IN100, *Int. J. Plast.* 26 (2010) 372–394. doi:10.1016/j.ijplas.2009.08.001.
- [23] C.P. Przybyla, D.L. McDowell, Microstructure-sensitive extreme-value probabilities of high-cycle fatigue for surface vs. subsurface crack formation in duplex Ti–6Al–4V, *Acta Mater.* 60 (2012) 293–305. doi:10.1016/j.actamat.2011.09.031.
- [24] C.A. Sweeney, W. Vorster, S.B. Leen, E. Sakurada, P.E. McHugh, F.P.E. Dunne, The role of elastic anisotropy, length scale and crystallographic slip in fatigue crack

- nucleation, *J. Mech. Phys. Solids.* 61 (2013) 1224–1240. doi:10.1016/j.jmps.2013.01.001.
- [25] A. Manonukul, F.P.E. Dunne, High- and low-cycle fatigue crack initiation using polycrystal plasticity, *Proc. R. Soc. Lond. Ser. Math. Phys. Eng. Sci.* 460 (2004) 1881 – 1903. doi:10.1098/rspa.2003.1258.
- [26] A.M. Korsunsky, D. Dini, F.P.E. Dunne, M.J. Walsh, Comparative assessment of dissipated energy and other fatigue criteria, *Int. J. Fatigue.* 29 (2007) 1990–1995. doi:16/j.ijfatigue.2007.01.007.
- [27] Y. Li, V. Aubin, C. Rey, P. Bompard, Microstructural modeling of fatigue crack initiation in austenitic steel 304L, *Procedia Eng.* 31 (2012) 541–549. doi:10.1016/j.proeng.2012.01.1065.
- [28] C.A. Sweeney, B. O’Brien, F.P.E. Dunne, P.E. McHugh, S.B. Leen, Strain-gradient modelling of grain size effects on fatigue of CoCr alloy, *Acta Mater.* 78 (2014) 341–353. doi:10.1016/j.actamat.2014.06.044.
- [29] M. Mineur, P. Villechaise, J. Mendez, Influence of the crystalline texture on the fatigue behavior of a 316L austenitic stainless steel, *Mater. Sci. Eng. A.* 286 (2000) 257–268. doi:16/S0921-5093(00)00804-2.
- [30] E. Donnelly, Geometry effect in the fatigue behaviour of microscale 316L stainless steel specimens, Thesis, 2012. <http://aran.library.nuigalway.ie/xmlui/handle/10379/3029> (accessed September 16, 2014).
- [31] P. Sojitra, C. Engineer, A. Rval, D. Kothwala, A. Jariwala, H. Kotadia, et al., Surface enhancement and characterization of L-605 cobalt alloy cardiovascular stent by novel electrochemical treatment, *Artif. Organs.* 23 (2009) 55–64.
- [32] H. Aihara, Surface and biocompatibility study of electropolished Co-Cr alloy L605, Thesis, San Jose State University, 2009.
- [33] S.K. Sudheer, D. Kothwala, S. Prathibha, C. Engineer, A. Raval, H. Kotadia, Laser microfabrication of L605 cobalt-chromium cardiovascular stent implants with modulated pulsed Nd:YAG laser, *J. MicroNanolithography MEMS MOEMS.* 7 (2008) 033012–1–033012–9. doi:10.1117/1.2965539.
- [34] C. Kaufmann, G. Mani, D. Marton, D. Johnson, C.M. Agrawal, Long-term stability of self-assembled monolayers on electropolished L605 cobalt chromium alloy for stent applications, *J. Biomed. Mater. Res. B Appl. Biomater.* 98 (2011) 280–289. doi:10.1002/jbm.b.31850.
- [35] Y. Huang, A user-material subroutine incorporating single crystal plasticity in the Abaqus finite element program, Harvard University, 1991.
- [36] D. Peirce, R. Asaro, A. Needleman, An analysis of nonuniform and localized deformation in ductile single crystals, *Acta Metall.* 30 (1982) 1087–1119. doi:10.1016/0001-6160(82)90005-0.
- [37] R.J. Asaro, Micromechanics of Crystals and Polycrystals, *Adv. Appl. Mech.* 23 (1983) 1–115. doi:10.1016/S0065-2156(08)70242-4.
- [38] R.J. Asaro, Crystal plasticity, *J. Appl. Mech.* 50 (1983) 921–934. doi:10.1115/1.3167205.
- [39] P.E. McHugh, R.J. Asaro, C.F. Shih, Computational modeling of metal matrix composite materials—I. Isothermal deformation patterns in ideal microstructures, *Acta Metall. Mater.* 41 (1993) 1461–1476. doi:10.1016/0956-7151(93)90255-Q.
- [40] F.P.E. Dunne, R. Kiwanuka, A.J. Wilkinson, Crystal plasticity analysis of micro-deformation, lattice rotation and geometrically necessary dislocation density, *Proc. R. Soc. Math. Phys. Eng. Sci.* 468 (2012) 2509–2531. doi:10.1098/rspa.2012.0050.

- [41] P. Connolly, P.E. McHugh, Fracture modelling of WC-Co hardmetals using crystal plasticity theory and the Gurson model, *Fatigue Fract. Eng. Mater. Struct.* 22 (1999) 77–86. doi:10.1046/j.1460-2695.1999.00153.x.
- [42] V.V.C. Wan, D.W. MacLachlan, F.P.E. Dunne, A stored energy criterion for fatigue crack nucleation in polycrystals, *Int. J. Fatigue.* 68 (2014) 90–102. doi:10.1016/j.ijfatigue.2014.06.001.
- [43] A.K. Wong, G.C. Kirby III, A hybrid numerical/experimental technique for determining the heat dissipated during low cycle fatigue, *Eng. Fract. Mech.* 37 (1990) 493–504. doi:10.1016/0013-7944(90)90375-Q.
- [44] G. Meneghetti, M. Ricotta, The use of the specific heat loss to analyse the low- and high-cycle fatigue behaviour of plain and notched specimens made of a stainless steel, *Eng. Fract. Mech.* 81 (2012) 2–16. doi:10.1016/j.engfracmech.2011.06.010.
- [45] F.P.E. Dunne, D. Rugg, On the mechanisms of fatigue facet nucleation in titanium alloys, *Fatigue Fract. Eng. Mater. Struct.* 31 (2008) 949–958. doi:10.1111/j.1460-2695.2008.01284.x.
- [46] C. Przybyla, R. Prasannavenkatesan, N. Salajegheh, D.L. McDowell, Microstructure-sensitive modeling of high cycle fatigue, *Int. J. Fatigue.* 32 (2010) 512–525. doi:10.1016/j.ijfatigue.2009.03.021.
- [47] J. Schwartz, O. Fandeur, C. Rey, Fatigue crack initiation modeling of 316LN steel based on non local plasticity theory, *Procedia Eng.* 2 (2010) 1353–1362. doi:10.1016/j.proeng.2010.03.147.
- [48] G.M. Castelluccio, D.L. McDowell, Effect of annealing twins on crack initiation under high cycle fatigue conditions, *J. Mater. Sci.* 48 (2013) 2376–2387. doi:10.1007/s10853-012-7021-y.